International Comparison CCQM-P229: Pilot Study to Measure Line Intensities of Selected $^{12}C^{16}O$ Transitions

Final Report Summary

Joseph T. Hodges,[1] Katarzyna Bielska,[2] Manfred Birk,[3] Roman Ciuryło,[2] Agata Cygan,[2] Vittorio D'Agostino,[2,4] Ruimin Guo,[5] Gang Li,[6] Jeong Sik Lim,[7] Daniel Lisak,[2] Zachary Reed,[1] Georg Wagner[3], Szymon Wójtewicz[2]

[1]*National Institute of Standards and Technology (NIST), 100 Bureau Drive, Gaithersburg, MD 20899, United States of America*
[2]*Institute of Physics, Faculty of Physics, Astronomy and Informatics, Nicolaus Copernicus University in Toruń, Grudziadzka 5, 87-100, Toruń, Poland*
[3]*Remote Sensing Technology Institute, German Aerospace Center (DLR), D-82234 Wessling, Germany*
[4]*Department of Mathematics and Physics, Università degli Studi della Campania ''Luigi Vanvitelli'', 81100, Caserta, Italy*
[5]*Center for Environmental Metrology, National Institute of Metrology, Beijing, China 100029*
[6]*Physikalisch-Technische Bundensanstalt, Bundesallee 100, 38116 Braunschweig, Germany*
[7]*Research Center for Climate Metasphere, KRISS, 267 Gajeong-Ro, Yuseong-gu, Daejeon 34113, Republic of Korea*

Field
Amount of substance

Subject
Comparison of absolute molecular line intensities of the type used as the basis for spectroscopic measurements of amount of substance.

Abstract: We present primary spectroscopic measurements of line intensities in the 3-0 vibrational band of $^{12}C^{16}O$. This international measurement campaign was organized under the auspices of the Consultative Committee for Amount of Substance (CCQM) and involved six laboratories carrying out independent measurements of more than forty rotation-vibration transitions. A total of three measurement techniques on samples of pure carbon monoxide were applied in this intercomparison, including Fourier transform spectroscopy, cavity ring-down spectroscopy, and cavity mode dispersion spectroscopy. Using advanced spectroscopic line shape models and thorough characterization of instrument response to analyze the measured spectra, artifact-free measurements of line intensities were obtained by each laboratory. Average intensities were weighted by the inverse of the combined variance determined from rigorous estimates of combined systematic and statistical uncertainties. Results for all lines from five of the laboratories were scattered about the weighted mean value by nominally one part per thousand. Comparison of the weighted integrated band intensity with quantum-chemical calculations differed by nominally one part per ten thousand, thus demonstrating excellent agreement between experiment and theory. These results serve as an experimental benchmark for assessing the uncertainty in theoretical calculations, and they reveal the benefits of coordinated experiments that leverage complementary and independent primary measurements from contributing laboratories.

1 Introduction

This pilot study is the first of its type involving independent measurements of molecular line intensities for carbon monoxide (CO). These intensities can subsequently be used to determine CO amount of substance

J.T. Hodges et al., 2025 *Metrologia* **62** 08006.
DOI 10.1088/0026-1394/62/1A/08006

using linear absorption spectroscopy. To this end, each participant chose a specific technique and measured overlapping sets of rotation-vibration transitions within the 3-0 vibrational band of the $^{12}C^{16}O$ isotopologue. Using the protocol discussed below in Sec. 2.3, it was possible to investigate systematic biases between the various experimental techniques implemented by the participants and to make direct comparisons with theory. Also, to minimize uncertainties originating from the use of diluted sample gases all gas samples were nominally pure CO at near natural isotopic abundance measured near room temperature and corrected to a reference temperature of 296 K using the known partition function of $^{12}C^{16}O$ and lower-state energy for each transition. CO was chosen as a nearly ideal candidate for this study given the relatively low density of transitions, its low affinity to stick to chamber walls, and the accuracy with which intensities of this diatomic molecule can be determined from semi-empirical potential energy determinations and quantum-chemical calculations of transition moments.

2 Design and organization of the pilot study

2.1 Participants

Table 1: List of participants

Acronym	Country	Institute
DLR	DE	German Aerospace Center (DLR), Remote Sensing Technology, Institute, D-82234, Wessling, Germany
KRISS	KR	Korea Research Institute of Standards and Science, Research Cneter for Climate Metasphere, Deajeon, Republic of Korea
NCU	PL	Nicolaus Copernicus University in Toruń, Faculty of Physics, Astronomy and Informatics, Institute of Physics, Toruń, Poland
NIM	CN	National Institute of Metrology, Center for Environmental Technology, Beijing China, 100029
NIST	US	National Institute of Standards and Technology, Chemical Science Division, Gaithersburg, United States of America
PTB	DE	Physikalische-Technische Bundesanstalt, Braunschweig, Germany

2.2 Measurement Objectives

The principal objective was to quantify the degree of equivalence between SI-traceable spectroscopic measurements of CO line intensities made without reference to calibration gas mixtures. To this end, we chose to include independent and distinct experimental methods that are subject to differing biases, and we compared the measured CO intensities to the most advanced *ab initio* quantum-chemical calculations of CO intensities. Further, our goal was for these measured intensities (which are based on intrinsic molecular properties of the light-absorbing species) to enable subsequent SI-traceable measurements of CO amount fraction (using linear spectroscopic methods such as those implemented herein) on CO-containing gas samples of unknown composition. In this fashion and more generally, the present CO study acts as a proxy for other molecules, demonstrating the quantitative potential of linear absorption spectroscopy for species-specific measurements of amount of substance.

With these goals in mind, one of three different experimental methods was selected by each participating laboratory: 1) Fourier transform spectroscopy (FTS) by DLR and PTB, 2) cavity ring-down spectroscopy (CRDS) by KRISS, NIM and NIST, and 3) cavity mode dispersion spectroscopy (CMDS) by NCU. Notably FTS has much higher detection limits than CRDS and CMDS, varying by about three orders of magnitude. Indeed, because of dynamic range considerations, prior to this study no direct comparisons of FTS and CRDS (or CMDS) measurements of the same CO transitions have been reported. This situation exists in part because of the difficulty of optimizing these methods for the measurement of the same gas composition. Here, we made concerted efforts to devise an experimental plan that allowed for some direct

overlap between all techniques, whereby the same transitions on pure samples near room temperature (but at variable pressure) were measured.

2.3 Measurement protocol

The protocol requested that each laboratory measure at least the following five $^{12}C^{16}O$ 3-0 band transitions comprising rotational quantum numbers [P20, P10, R7, R16, R23] for which accurate measurements were possible using the FTS, CRDS and CMDS techniques. To extend the range of comparison, we requested that a larger set of transitions be considered including [P22, P16, P1, R25, R28], the stronger of which would be readily measured by FTS and the weaker of which would be amenable to measurements using the more sensitive CRDS and CMDS techniques. We refer to the combination of these two sets as the "overlap set" comprising the transitions designated by [P22, P20, P16, P10, P1, R7, R16, R23, R25, R28]. In this fashion, the complete set of measured intensities would comprise at least ten transitions, spanning a range in magnitude of approximately 240:1. All measurements were to be made near T = 296 K, and corrected to this reference temperature using HITRAN 2020 values [1] for the total internal partition function, $Q(T)$, and lower-state energies, E". Participants were asked to provide uncertainty estimates covering all important contributions arising from statistical (Type A) and persistent or systematic (Type B) effects. Combined uncertainties were to be reported as standard (k=1) values. We stress that the experimental techniques discussed here are based on the absorption of light by matter and constitute primary methods for measuring amount of substance which can be traceable to the SI through observables having dimensions of time, frequency, length, pressure, and temperature.

2.4 Origin and schedule of the pilot study

The idea for the present pilot study can be traced to email correspondences in late 2019 between several members of the CCQM Gas Analysis Working Group (GAWG), including Ruimin Guo (NIM), Joseph T. Hodges (NIST), Sangil Lee (KRISS) and Paul Brewer (NPL). At that time, there was an emerging interest among this gas standards community to develop and apply primary linear spectroscopic methods for measuring amount of substance. These discussions led to the formation of a new task group within GAWG named the Task Group on Advanced Spectroscopy (TGAS) to be chaired by Joseph T. Hodges. First, a terms of reference (TOR) document for TGAS was drafted and eventually approved by the GAWG. In the TOR, it was proposed that the TGAS carry out the present pilot study involving participants from within GAWG as well as those from other expert laboratories. The purpose was to evaluate the feasibility of doing SI-traceable measurement of line intensities to enable primary spectroscopic measurements of amount of substance. To summarize the timeline involved in realizing this work, the resulting schedule is given in Table 2.

Table 2: Schedule of CCQM-GAWG pilot study P-229.

Date	Event
October 2021	Virtual kickoff meeting
May 2022	Terms of reference assigned
July 2022	First measurements completed
March 2023	Study number CCQM-P229 assigned
October 2023	Last measurements completed
December 2024	Final report

2.5 Measurement principle

Consider a transition between two molecular states specified by quantum numbers, η and η' caused by absorption of a photon having energy $h\nu_{\eta\eta'}$ at frequency, $\nu_{\eta\eta'}$ [Hz] , where h is the Planck constant, and

where η' and η refer to the upper and lower states, respectively [2]. Here, we assume that the state populations are in thermal equilibrium, and because of low photon fluence and/or rapid relaxation effects, radiation-induced changes in the relative state populations $f_\eta = n_\eta/n_a$ and $f_{\eta'} = n_{\eta'}/n_a$ (in which the quantity n_a[m^{-3}] is the total absorber number density) are assumed to be too small to alter the thermal equilibrium. This situation corresponds to the domain whereby the rate at which photons are absorbed per unit volume is linearly proportional to the radiation field energy density, I/c, in which I is the beam intensity [W m^{-2}] and c is the speed of light [m s^{-1}]. With these assumptions, the rate of photon absorption per unit volume per frequency interval is

$$\frac{dn_p}{dt} = \frac{I}{c} n_a (f_\eta g_\eta B_{\eta\eta'} - f_{\eta'} g_{\eta'} B_{\eta'\eta}) \Phi_R(\nu - \nu_{\eta\eta'}) , \quad (1)$$

in which $B_{\eta\eta'}$ [J^{-1} s^{-2} m^3] is the Einstein coefficient for absorption, $B_{\eta'\eta}$ [J^{-1} s^{-2} m^3] is the Einstein coefficient for stimulated emission, g_η and $g_{\eta'}$ are the degeneracies of states η and η' respectively. Here $\tilde{\Phi}(\nu - \nu_{\eta\eta'}) = \Phi_R + i\Phi_I$ [s] is the complex-valued line shape function, in which Φ_R and Φ_I are its real and imaginary parts. These functions describe the absorptive and dispersive spectral distributions of the transitions, respectively, and are connected through the Kramers-Kronig relations [3-6]. $B_{\eta\eta'}$ and $B_{\eta'\eta}$ are intrinsically related to each other and to the Einstein spontaneous emission coefficient, $A_{\eta'\eta}$ [s^{-1}] by

$$B_{\eta\eta'} = \frac{g_{\eta'}}{g_\eta} B_{\eta'\eta} = \frac{A_{\eta'\eta}}{8\pi h\nu_{\eta\eta'}} \frac{g_{\eta'}}{g_\eta} \frac{c^3}{\nu_{\eta\eta'}^2}, \quad (2)$$

in which

$$A_{\eta'\eta} = \frac{64\pi^4 \nu_{\eta\eta'}^3}{3hc^3} \frac{g_\eta}{g_{\eta'}} \mathcal{R}_{\eta\eta'} , \quad (3)$$

where $\mathcal{R}_{\eta\eta'}$ [J m^3] represents the weighted transition-moment-squared for the molecule [2]. Importantly, all quantities in Eqs. 2 and 3 are molecular constants and can be determined to varying degrees of accuracy using *ab initio* quantum calculations. Thus, the Einstein coefficients for absorption and stimulated emission are intrinsic properties of the isolated molecule and are independent of temperature and collisional partners. Physically, $B_{\eta\eta'}$ corresponds to the probability (per unit time per unit radiation energy density per unit frequency) that absorption of a photon of energy $h\nu_{\eta\eta'}$ will cause the molecule to go from state η to η'. We note that $B_{\eta'\eta}$ is the analogous probability for stimulated emission corresponding to transition from state η' to η.

Multiplying both sides of Eq. 1 by $h\nu_{\eta\eta'}$ [J], and considering a beam of light with cross-sectional area, A_b, propagating along the *z*-direction, then we can write $P(z) = I(z)A_b$ in which $P(z)$ [W] is the beam power along the light path. Defining the differential volume, $dV = A_b dz$, we arrive at the well-known linear differential equation upon which the Beer-Lambert law (sometimes referred to as the Bouguer law) of absorption is based [7]:

$$\frac{dP(z)}{dV} = \frac{A_b dI}{A_b dz} = \frac{dI}{dz} = -\frac{I(z)}{c} h\nu_{\eta\eta'} n_a (f_\eta g_\eta B_{\eta\eta'} - f_{\eta'} g_{\eta'} B_{\eta'\eta}) \Phi_R(\nu - \nu_{\eta\eta'}) . \quad (4)$$

Defining the absorption coefficient, α [m^{-1}], as $-\frac{dln(I)}{dz}$, and substituting into Eq. 4 we obtain,

$$\alpha(\nu) = \frac{h\nu_{\eta\eta'}}{c} (f_\eta g_\eta B_{\eta\eta'} - f_{\eta'} g_{\eta'} B_{\eta'\eta}) n_a \Phi_R(\nu - \nu_{\eta\eta'}) = S(T) n_a \Phi_R(\nu - \nu_{\eta\eta'}). \quad (5)$$

The second equality above relates the line intensity, $S(T)$, to the absorption coefficient, temperature, absorber number density and line shape of the transition: all of which are experimental observables.

Focusing on the theoretical expression for the line intensity, we assume that at thermal equilibrium the fractions of all absorber molecules in states η and η' are

$$f_\eta = \frac{n_\eta}{n_a} = \frac{e^{-\frac{E_\eta}{kT}}}{Q(T)}, \tag{6}$$

$$\text{and } f_{\eta'} = \frac{n_{\eta'}}{n_a} = \frac{e^{-\frac{E_{\eta'}}{kT}}}{Q(T)}, \tag{7}$$

where the dimensionless function $Q(T)$ is the total internal partition function of the absorbing molecule, E_η [J] and $E_{\eta'}$ [J] are the energies of the lower and upper states, respectively, and k [J K^{-1}] is the Boltzmann constant. Using Eqs. 2 and 3 connecting the Einstein coefficients and the relation $E_{\eta'} - E_\eta = h\nu_{\eta\eta'}$ the definition of the line intensity, $S_{\eta\eta'}(T)$, [m^2 s^{-1}] can be written as the product of an intrinsic part and two temperature-dependent parts equal to

$$S_{\eta\eta'}(T) = \left[\frac{g_\eta A_{\eta\eta'}}{8\pi}\frac{c^2}{\nu_{\eta\eta'}{}^2}\right]\left[\frac{e^{-\frac{E_\eta}{kT}}}{Q(T)}\right][1 - e^{-\frac{h\nu_{\eta\eta'}}{kT}}], \tag{8}$$

where from left to right the three bracketed terms represent the intrinsic component, the Boltzmann population factor for the lower state, and the net reduction in absorption caused by stimulated emission from the upper state population, respectively. At room temperature and optical frequencies, this last term is essentially unity.

Returning to the relation $\alpha(\nu - \nu_{\eta\eta'}) = n_a S_{\eta\eta'}(T)\,\Phi_R(\nu - \nu_{\eta\eta'})$ it is understood that the integral over frequency detuning of the real part of the line shape function is normalized so that $\int_{-\infty}^{\infty}\Phi_R(\nu - \nu_{\eta\eta'})\,d\nu = 1$. With this normalization the integral of the observed spectrum over all frequencies yields the peak area given by,

$$a_{\eta\eta'} = \int_{-\infty}^{\infty}\alpha(\nu - \nu_{\eta\eta'})d\nu = n_a S_{\eta\eta'}(T) = [\chi_a p/(kT)]S_{\eta\eta'}(T). \tag{9}$$

Here we use the ideal gas law to give the number density, and we specify χ_a as the amount fraction of the absorber in the gas mixture (a quantity that must incorporate the relative isotopologue abundance). Corrections for real-gas effects can be readily incorporated into the calculation of n_a.

For measurements of mode dispersion (*e.g.*, CMDS method considered in this study), $\Delta\nu_D(\nu - \nu_0)$ [Hz], one can derive an expression analogous to Eq. 9 which links the observable to the product of line intensity and the imaginary component of the line shape function. The derivation reduces to,

$$\Delta\nu_D(\nu - \nu_{\eta\eta'}) = \frac{1}{4\pi n_0} c n_a S_{\eta\eta'}(T)\Phi_I(\nu - \nu_{\eta\eta'}), \tag{10}$$

where n_0 is the real part of the refractive index of the medium.

We note that per-molecule line intensities are typically expressed in units of [cm^2 cm^{-1}] (e.g., HITRAN), which can be obtained by dividing the right-hand side of Eq. 8 by the constant factor *c*. We follow this convention in the remainder of this report.

In practice data reduction of measured absorption spectra (CRDS or FTS) and dispersion spectra (CMDS) methods both yield the product $n_a S_{\eta\eta'}(T)$. This type of analysis generally requires fitting parameterized line shape models used in Eqs. 5 or 10 to measured values of $\alpha(\nu - \nu_{\eta\eta'})$ or $\Delta\nu_d(\nu - \nu_{\eta\eta'})$, respectively. To compare intensity data from different measurements, Eq. 8 is used to convert $S_{\eta\eta'}(T)$ to $S_{\eta\eta'}(T_r)$, where the reference temperature, T_r, is arbitrarily assigned to be 296 K. Typically, $\widetilde{\Phi}(\nu - \nu_{\eta\eta'})$ is modelled using

standardized spectroscopic profiles such as the Hartmann-Tran (HT) profile and its other limiting cases [8, 9]. Parameters for the HT include the Doppler and Lorentzian widths, Dicke narrowing frequency, speed dependence parameter, among others.

2.6 Measurement overview

Details regarding the spectroscopic measurement techniques used by the participants are described in the Supplemental Material (SM). Table 3 lists these methods, acquisition dates, number of lines, pressure range, and sample volume dimensions.

Table 3: Overview of experimental schedule, methods, and sample conditions

Laboratory	Acquisition Dates	Spectroscopic Technique	Number of Lines	Pressure Range (kPa)	Sample Volume (cm^3)
DLR	May - June 2022	FTS	48	0.5 – 50.0	16000
KRISS	Aug. 2023	CRDS	4	1.9 – 6.0	9000
NCU	April - June 2023	CMDS	10	0.03 – 20.0	200
NIM	Dec. 2022 – Feb. 2023	CRDS	10	0.002 – 2.00	169
NIST	Mar. – Aug. 2023	CRDS	10	0.003 – 0.83	400
PTB	Feb. 2018	FTS	45	10.2	20360

All laboratories measured room-temperature samples of high-purity carbon monoxide (CO). See Table 4 for purity specifications and estimates of the $^{12}C^{16}O$ isotopologue amount fraction. The measurement techniques include Fourier transform spectroscopy (FTS) [10, 11], cavity ring-down spectroscopy (CRDS) [12], and cavity mode dispersion spectroscopy (CMDS) [13].

In Table 8.1 of the SM we list the set of $^{12}C^{16}O$ (3-0) band transitions considered as well as the transition frequencies, and lower-state energies used for temperature normalization, while theoretical intensities, $S^{(t)}$, used as reference values are given in Table 8.2 of the SM. In our notation each line is labelled by the quantum number, m, defined as $-J$ for P-branch ($\Delta J = -1$) lines, and $J + 1$ for those in the R-branch ($\Delta J = 1$), where J is the ground-state rotational quantum number within the $^{12}C^{16}O$ (3-0) vibrational band. Note that there were at least at least two independent measurements from different laboratories for all lines considered here. Furthermore, the number of laboratories, N_L, that contributed results varied from line to line.

2.6 Isotopic composition and purity of sample gases

To account for small deviations from unity in the $^{12}C^{16}O$ amount fraction, all laboratories specified the carbon monoxide purity, f_{CO}, and the relative abundance of this isotopologue, χ_{26}. See Table 4 for a summary of these values and relative uncertainties for each laboratory. The final intensities correspond to 100 % $^{12}C^{16}O$ and were evaluated by dividing the measured values by the corresponding product $f_{CO}\ \chi_{26}$. The average relative deviation in χ_{26} (excluding the KRISS results) with respect to the HITRAN 2020 [14] reference value was 0.48 ‰ with a maximum difference of 0.56 ‰. As shown below, failure to account for these slight differences in composition would lead to a bias that is comparable in magnitude to the overall measurement precision, thus making this an important correction factor. Details regarding the determination of the isotopic composition of the CO samples for each laboratory are discussed in the SM.

Table 4. Specifications for the CO sample gases used by each participating laboratory. f_{CO} is the manufacturer's stated purity for the carbon monoxide sample, and Δ_{26} is the relative difference between the measured χ_{26} and the HITRAN 2020 [14] reference value, $\chi_{26,HT} = 0.986544$. Values of χ_{26} were determined spectroscopically by measuring spectral area ratios from pairs of isotopologues or by using isotope ratio mass spectrometry. Details regarding these measurements are discussed in the SM.

laboratory	f_{CO}	χ_{12C16O}	$u_r(\chi_{12C16O})$ (‰)	Δ_{26} (‰)	method
DLR	0.999970	0.986843	0.12	0.30	absorption spectroscopy
KRISS	0.999980	0.986544	-	0	HITRAN value for χ_{12C16O}
NCU	0.999970	0.987175	0.12	0.72	absorption spectroscopy
NIM	0.999988	0.986721	0.01	0.18	mass spectrometry
NIST	0.999950	0.986904	0.12	0.45	absorption spectroscopy
PTB	0.999995	0.987275	0.12	0.74	absorption spectroscopy

2.7 Other sources of uncertainty

Additional uncertainty components considered include those related to measurements of pressure, temperature, absorption pathlength, instrumental line shape, peak area determination from fit of spectroscopic model, as well as nonidealities caused by detector and digitizer nonidealities. We note that for the optical-resonator-based measurements (CRDS and CMDS), optical pathlength within the absorption cell need not be determined explicitly because the absorption coefficient is inferred from observations of time and frequency. For the two FTS-based experiments, pathlengths were measured using redundant and precisely characterized mechanical tolerances, laser-ranging methods, and ray tracing analysis. See SM for more details.

3 Results

3.1 Averaging and weighting of the data

Tables 9.1a and 9.1b in the SM give the reported intensities and the relative combined standard uncertainties from each laboratory. Details regarding assessment of these uncertainties are presented in the SM.

To compare the results, we begin by evaluating a weighted-mean intensity, $\overline{S}_m$, for each line, where the average includes all contributing laboratories. For a given m, we assume normally distributed, uncorrelated and nonuniform uncertainties for each laboratory datum, labelled by the index, i. Each resulting weighting factor, $w_i(S_{i,m})$, was evaluated in terms of the reported relative combined standard uncertainty, so that it is [15]:

$$w_i = u_{r,i}^{-2} / \sum_i^{N_L(m)} u_{r,i}^{-2}, \tag{11}$$

giving

$$\overline{S}_m = \frac{\sum_i^{N_L(m)} S_{i,m} u_{r,i}^{-2}}{\sum_i^{N_L(m)} u_{r,i}^{-2}}, \tag{12}$$

for which the relative uncertainty in each mean value was computed as a standard error by

$$u_r(\overline{S}_m) = \left(\frac{1}{\sum_i^{N_L(m)} u_{r,i}^{-2}} \right)^{1/2}, \tag{13}$$

in which we interpret the standard error as the standard uncertainty in $\overline{S}_m$, not to be confused with the sample standard deviation [16].

3.2 Comparison of measurements and statistical analysis

To compare the results from all six participating laboratories we evaluate the relative difference between each experimental datum, $S_{i,m}$, and the corresponding weighted-mean value, $\overline{S}_m$, as, $\epsilon_{i,m} = (S_{i,m} - \overline{S}_m)/\overline{S}_m$. See Table 8.2 of the SM for the $\overline{S}_m$ and $u_r(\overline{S}_m)$ results and the corresponding theoretical intensity values discussed below. The upper panel of Fig. 1 shows these normalized intensity data for all laboratories where the indicated uncertainties are based primarily on those reported by each laboratory. The standard deviation of the set of $\epsilon_{i,m}$ data provides a measure of consistency between the reported intensities. Unfortunately, we note that the set of five intensities reported by KRISS (m = -22, 24, 26, 29), are clearly outliers given their large uncertainties and large deviations about the weighed mean values. Reasons for this discrepancy between the KRISS results and those from the remaining laboratories are discussed in the SM. To optimize the data analysis, the KRISS data are henceforth disregarded in the present analysis.

The lower panel of Fig. 1 provides a closer look at the spread in the measured intensities. Notably, the set of $\epsilon_{i,m}$ from DLR and PTB show opposite m-dependent deviations that can be explained in terms of systematic uncertainty in temperature as discussed in Sec. 7 of the SM. Also, the data from PTB indicate a "dip" about m = 0, the origin of which will be discussed below.

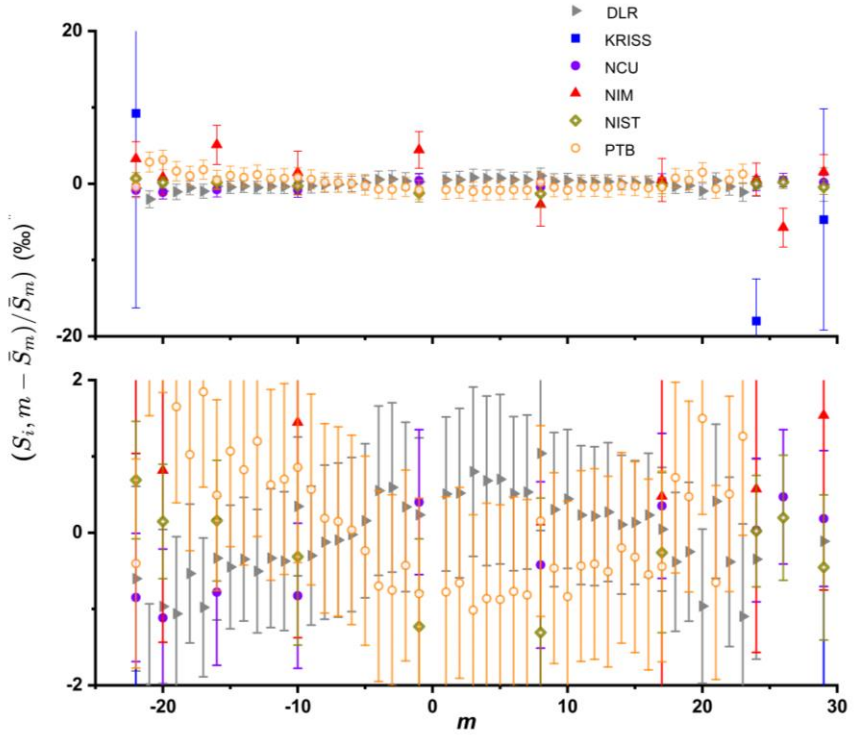

Figure 1. Relative differences between the measured intensities, $S_{i,m}$, (given in Tables 9.1a and 9.1b of the SM) and the weighted-mean intensity values (given in Table 8.2 of the SM) *vs*. the rotational quantum number, m. The lower panel is a tenfold zoom of the upper panel.

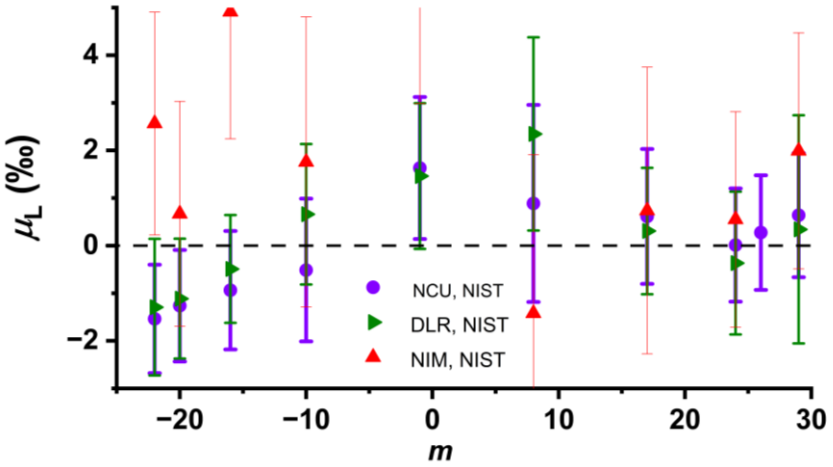

Figure 2. Unweighted relative differences, μ_L, between intensity results from DLR, NCU and NIM with respect to NIST measurements for lines in the overlap set.

In Fig. 2 we present another perspective of the dispersion in the measurements by focusing on the set of overlap set lines. This comparison shows the unweighted relative differences in intensity of the DLR, NCU and NIM intensities with respect to the NIST values. These data are evaluated as $\mu_L(m) = 2(S_{m,L} - S_{m,NIST})/(S_{m,L} + S_{m,NIST})$, in which the index, L, indicates DLR, NCU, or NIM. In the P branch region ($m < 0$), μ_{NCU}(m) and $\mu_{DLR}(m)$ are quite similar (average difference of 0.37 ‰), and both show the same linear trend with respect to the NIST results for the five P branch lines. This result suggests a systematic m-dependent effect in the NIST results. However, for the R16, R23, R25, and R28 lines, $\mu_{DLR}(m)$ and $\mu_{NCU}(m)$ vary randomly, with a maximum relative difference of 0.64 ‰ and a standard deviation of 0.35 ‰, (although we note that DLR did not report an intensity for the R25 line). For all overlap transitions in Fig. 2 (excluding the R25 line outlier from NIM), the average of $\mu_{DLR}(m)$, $\mu_{NCU}(m)$ and $\mu_{m,NIM}(m)$ (metric 1a) is 0.68 ‰ with a standard deviation of 1.73 ‰ (metric 1b). See Table 5 for a summary of these and additional statistical metrics to follow. We also point out (as discussed in Sec. 5.2 of the SM) that the intensities of the R7 and P10 transitions reported by NIST may have been underreported by about 0.5 ‰ because of leakage effects encountered at low measurement pressure (< 6 Pa).

Returning to the weighted intensity deviation results of Fig. 1, the standard deviation of the set of $\epsilon_{i,m}$ values (metric 2a) is 1.19 ‰, with a standard error of 0.11 ‰ (metric 2b) based on the ensemble of 122 measurements. See Fig. 3a for a histogram of these deviations and fitted normal distribution. Considering only the set of ten transitions in the overlap set m = [-22, -20, -16, -10, -1, 8, 17, 24, 26, 29] where most of the laboratories contributed measurements and for which there were at least two measurement techniques employed, the standard deviation of the $\epsilon_{i,m}$ values is 1.66 ‰ (metric 3a) with a standard error of 0.23 ‰ (metric 3b). Consistent with the increased average number of laboratories involved per line in the overlap set, this spread is slightly larger than that based on all the measured lines. However, the relative uncertainties, $u_r(\overline{S}_m)$, in the overlap set intensities are nearly 30 % smaller than those of the remaining lines which comprise only FTS measurements from DLR and PTB. As can be seen in Fig. 4, the resulting weighting factors for the ten lines in the overlap set are about twice as large as those of the remaining lines.

This result illustrates the benefit of combining data from independent data sources to reduce overall uncertainty.

Table 5: Summary of the analysis metrics.

metric ID	description	ensemble	‰
1a	average of deviations with respect to NIST data for $\mu_{DLR}(m)$, $\mu_{NCU}(m)$ and $\mu_{NIM}(m)$	overlap set	0.68
1b	standard deviation of metric 1a	overlap set	1.73
2a	standard deviation of the set of relative differences, $\epsilon_{i,m}$, between the experimental and weighted-mean intensities	all m	1.19
2b	standard error of metric 2a; $\sigma_\epsilon/n^{1/2}$ where n = 122	all m	0.11
3a	standard deviation of the set of relative differences, $\epsilon_{i,m}$, between the experimental and weighted-mean intensities	overlap set	1.66
3b	standard error of metric 3a; $\sigma_\epsilon/n^{1/2}$, where n = 50	overlap set	0.23
4a	average of the set of relative differences, δ_m, between the weighted-mean experimental intensities and theory	all m	-0.15
4b	standard deviation, σ_δ, of the set of δ_m	all m	0.58
4c	standard error of metric 4a; $\sigma_\delta^{(fit)}/n^{1/2}$, where n = 48	all m	0.08
5a	(measured – theoretical) integrated band intensity based on $\delta_m^{(fit)}$	all m	0.13
5b	standard deviation, $\sigma_\delta^{(fit)}$, in residuals of $\delta_m^{(fit)}$ for integrated band intensity.	all m	0.31
5a	standard error in band intensity based on $\delta_m^{(fit)}$; $\sigma_\delta^{(fit)}/n^{1/2}$, where n = 48	all m	0.04

DOI 10.1088/0026-1394/62/1A/08006

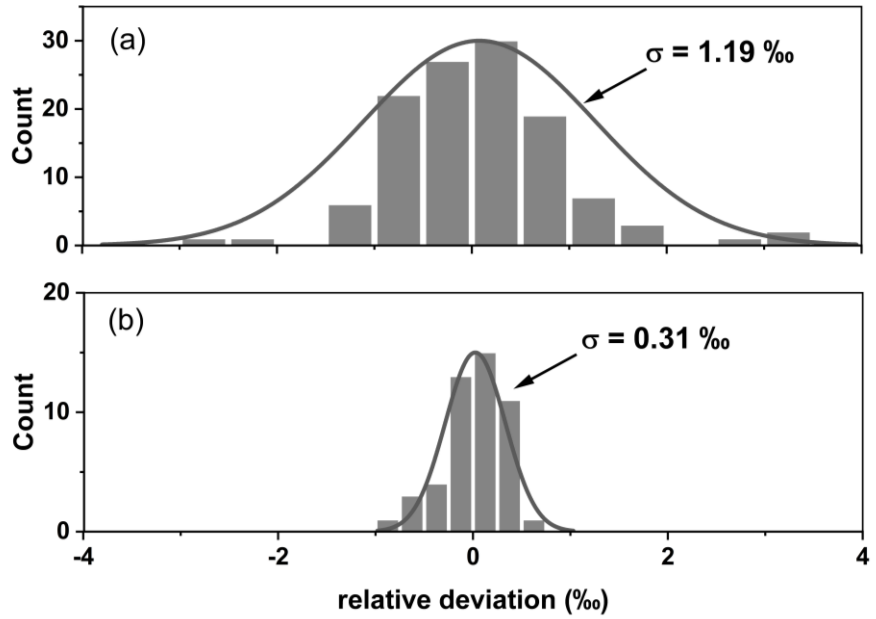

Figure 3. (a) Distribution of the relative deviation, $(S_{i,m}/\bar{S}_m - 1)$, corresponding to each measured intensity about its respective weighted mean value (no KRISS data). (b) Distribution of the fit residuals shown in Fig. 5. The black curves represent fits of normal distribution to each set of data, resulting in standard deviations of 1.19 ‰ and 0.31 ‰, respectively. Both ensembles consist of 122 observations.

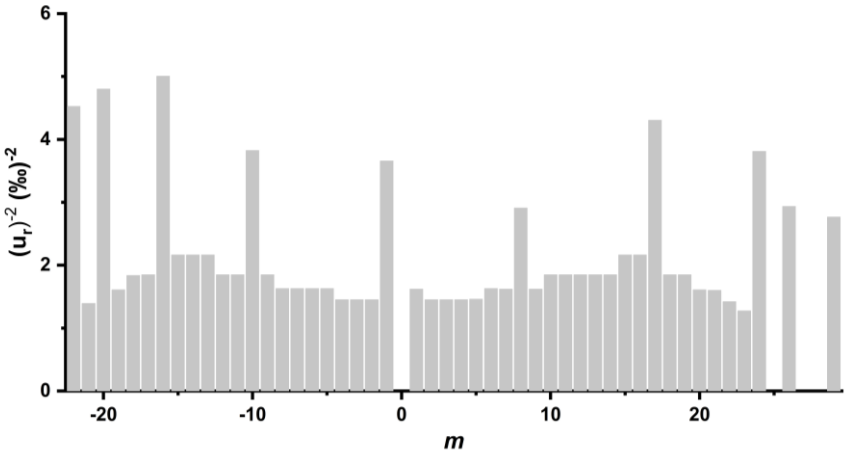

Figure 4. Weighting factors of each mean transition intensity, $\bar{S}_m$. These were obtained from the reciprocal relative combined standard uncertainties of measured intensities from Eq. 13 after combining data from all contributing laboratories.

3.3 Comparison of weighted-mean intensities with theory

We also compared our weighted-mean measured intensities to theoretical values using a high-accuracy *ab initio* dipole moment curve and a semi-empirical potential energy curve similar to those recently discussed by Polyansky and coworkers in a global analysis of CO band [17]. The present theoretical intensities are restricted to those for the 3-0 band of $^{12}C^{16}O$ (see Bielska *et al*. [18] and Table 8.2 of the SM)). As reported by Bielska *et al*. [18], agreement between experiment and theory for the $^{12}C^{16}O$ 3-0 band intensities was at the sub-1 ‰ level. These previous experimental results comprised data from three groups in the present study: NIST, PTB and NCU.

In Fig. 5 we plot the weighted-mean intensity, $\bar{S}_m$ relative to the corresponding theoretical value, $S_m^{(t)}$, at each *m*, which we define as $\delta_m = (\bar{S}_m - S_m^{(t)})/S_m^{(t)}$. The error bars on this quantity are the same as those used to compute the weighting factors shown in Fig. 4. The average fractional difference between experiment and theory, δ_m, is -0.15 ‰ (metric 4a) with a standard deviation of 0.58 ‰ (metric 4b) and a standard error of 0.08 ‰. We note that these figures-of-merit are based on the total ensemble of lines considered here and can be affected by persistent *m*-dependencies in the sets of $\bar{S}_m$ and $S_m^{(t)}$. Indeed, inspection of the δ_m results in Fig. 5 reveals systematic *m*-dependent deviations between theory and experiment which span ±1 ‰. Moreover, there is a narrow "dip" at band center superimposed on a broader background. We expect that this feature is unlikely to be associated with the theoretical line intensity calculation, but rather we consider it as an experimental artifact originating from at least three effects. The remainder of the deviation corresponding to the broad background can result from uncertainties in both the measurement and the theory.

For the first possible explanation of the dip at band center, we note that the finite duration of molecular collisions can lead to an apparent depletion of intensity as reported in [19] for N_2-broadened CO and $|m|$ values less than about seven. This effect modifies the core line shape, is pressure dependent (nominally 5%/MPa), decreases rapidly with $|m|$ and depends on the collision partner. We expect that the FTS measurements by DLR and especially PTB could be affected by this mechanism given the pressure ranges of these measurements,

Second, as noted above, NIST measurements of the P1 and R7 transitions were made at low pressures where residual leakage of ambient air likely introduced a slight negative bias in the observed intensities. See Sec. 5.2 of the SM.

A third explanation for the observed dip involves the temperature dependence of the line intensities, and the temperature biases encountered in each experiment. As *m* increases in magnitude the sign of the temperature derivative, $d(S_m/T)/dT$, (see Sec. 7 of the SM) changes from negative to positive for $J = 14$, which could lead to a narrow residual feature (a dip or a peak) at band center depending on the magnitudes and signs of the constituent temperature biases.

The effects of temperature biases between the contributing experiments must also be considered in analyzing the broader trends in δ_m. As is evident in Fig. 1, the PTB and DLR data diverge at large values of $|m|$ and have opposite slopes, indicating that there is a temperature difference between the two laboratories, with individual measurement biases (measured – actual) that are opposite in sign. This temperature effect increases with $|m|$, likely rendering it as the dominant source of measurement uncertainty for large $|m|$. For example, it would take only a 0.1 K temperature increase to cause a 1.4 ‰ relative change in the line intensity for the P22 line and a 2.2 ‰ change for the R28 line. Nevertheless, for the lines comprising the overlap set (only one of which is within the dip), we assume that the temperature biases from all the laboratories are uncorrelated and tend to cancel. The remaining nine lines in the overlap set average over the results from five laboratories and provide our best estimate of the mean intensities about which the $\delta_{m,}$ data vary randomly. Thus, we assume that smoothed deviations outside of the dip region are dominated by limitations of the theoretical calculations- precluding perfectly accurate predictions of band intensity and individual intensities. For lack of a better descriptor, we refer to the slowly varying component of the smooth curve in Fig. 5 as a Herman-Wallis-like term, commonly used to account for perturbations of intensity by rotation-vibration interactions in diatomic molecules [20].

Based on the foregoing arguments, we model the observed δ_m as the sum of the Herman-Wallis-like term, $f_{HW}(m)$ and an exponential term accounting for the dip at band center as,

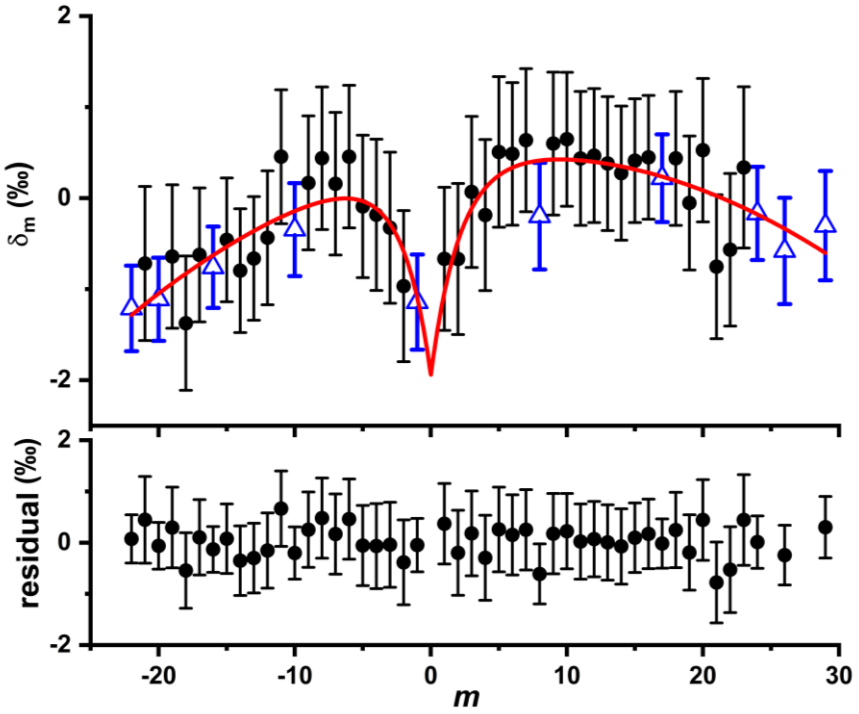

Figure 5. Upper panel: Relative differences, δ_m, between the mean intensities $\bar{S}_m$ based on this work, and theoretical intensities $S_m^{(t)}$, for the $^{12}C^{16}O$ (3-0) band reported in Bielska et al. [18]. The blue triangles and black circles correspond to the overlap set of lines and the FTS-only measurements, respectively. The red curve represents a least-squares fit of Eq. 14 to the data. Bottom panel: Fit residuals (measured – fitted).

$$\delta_m^{(fit)} = y_0 + f_{HW}(m) + f_{dip}(m) = y_0 + \beta(1 + a_1 m + a_2 m^2) - \eta e^{-|m|/w} \quad , (14)$$

where, y_0 , β, a_1, a_2, η and w are adjustable parameters. A weighted least-squares fit of this empirical equation to $\delta_m(m)$ gives y_0 = 0.30965, β = 0.06433, a_1 = 0.44011, a_2 = -0.03324, η = 2.31684, and w = 2.09251. The fit residuals are shown in the bottom panel of Fig. 5 and have a standard deviation equal to 0.31 ‰. A histogram of these residuals and fitted normal distribution are shown in Fig. 3b. Notably, this distribution is three times smaller than that based on the mean of the weighted normalized intensities in Fig. 3a. We attribute this improved precision to the data weighting and to the inclusion of the multiple sources of data with uncorrelated biases.

With the caveat that the broad background component to δ_m can be ascribed solely to limitations of the theory, then we can use $y_0 + f_{HW}(m)$ to represent the fitted relative difference between the (dip-corrected) experiment and theory. This assignment allows us to evaluate the individual measured and fitted line intensities, $S_m^{(fit)}$, as

$$\delta_m^{(fit)} - \eta e^{-|m|/w} = y_0 + f_{HW}(m) = (S_m^{(fit)} - S_m^{(t)})/S_m^{(t)} \quad , \quad (15)$$

which for the considered lines can be readily solved for $S_m^{(fit)}$. See Table 8.2 of the SM for these smoothed intensity values. This analysis yields a fitted band intensity of 4.7374×10^{-22} cm^2 cm^{-1}/molecule which is

0.13 ‰ (metric 5a) greater than the theoretical value of 4.7368×10^{-22} cm^2 cm^{-1}/molecule. Further, based on the standard deviation of the fit residuals (0.31 ‰; metric 5b) and the ensemble size (n = 48), the measured/theoretical band intensity ratio has a relative standard error of 0.04 ‰ (metric 5c).

The corrections to the $^{12}C^{16}O$ relative abundances (see Δ terms in Table 4), which account for heterogeneity in the isotopic composition of the CO samples, had a large impact on the resulting band intensity. These corrections range from 0.18 ‰ to 0.74 ‰. Being greater than 0, these corrections all correspond to enrichment in χ_{12C16O} and therefore they reduce the measured intensities. Without isotopic corrections, the relative difference between the experimental and theoretical band intensities would be 0.51 ‰: nearly a factor of four times greater than the corrected value of 0.13 ‰ (metric 5a):

4 Conclusions and recommendations

This pilot study demonstrates the feasibility of making exceptionally accurate and precise determinations of molecular line intensities (< 1 ‰ relative uncertainty level) through coordinated experiments that leverage complementary and independent primary measurements from contributing laboratories. The consistency between experiments was enabled by including several participants, thorough assessments of combined uncertainty, and a coordinated experimental design, all of which contributed to the precise assessment of differences between experiment and theory.

Experiments of this type are essential as benchmarks for predictive quantum-chemical calculations requiring experimental confirmation, yet which can be readily extended to cover a much broader range of transitions, bands, molecules, thermodynamic conditions *etc*. than can be readily achieved from experiments alone. The CO band discussed here also serves as a reference case to which experimentalists using a variety of independent spectroscopic methods can compare their results and establish confidence in their assigned measurement uncertainties. Given that we have demonstrated 0.13 ‰-level agreement between experiment and theory (over the range m = -22 to 29), we recommend that the theoretical intensities first reported in [18] and tabulated Table 8.1 of the SM constitute this reference line list.

We emphasize that use of this line list alone is insufficient to ensure traceability in absorption-based measurements- rather the specific implementation must involve a rigorous uncertainty analysis of all experimental observables. Nevertheless, line intensities that are grounded in experiment and theory, can serve as "rulers" for amount of substance, given that the transition moments underpinning the intensities are intrinsic molecular properties. In this way, linear absorption spectroscopic measurements linked to observations of time, frequency, pressure and temperature, and *a priori* intensities (from experiment and theory) can constitute artifact-free primary measurements of amount of substance.

Extension to other bands of CO as well as to other molecular bands that are amenable to line-by-line analysis should make possible continued advances in primary spectroscopic measurements of amount of substance, partial pressure, temperature, and isotopologue ratios. Indeed, there are many molecular species of interest to the gas analysis community with strong absorption bands that could be measured in a similar fashion. These include H_2O (1.4 μm), CO_2 (1.6 μm), 2.0 μm), N_2O (1.6 μm), CH_4 (1.65 μm), CH_2O (3.6 μm), NO (2.7 μm), NO_2 (3.4 μm), HCl (1.8 μm), HNO_3 (5.9 μm), all which of absorb electromagnetic radiation in spectral regions that can be readily accessed with existing laser/photonics technologies and traditional incoherent broadband methods.

Acknowledgments
The authors would like to thank Paul Brewer and Sangil Lee for encouraging us to implement this project under the auspices of the GAWG, Adriaan van der Veen, Stefan Persin and Edgar Flores for their comments on the manuscript, as well as all the respective institutions involved for their internal support. Daniel Lisak

and Katarzyna Bielska acknowledge partial support from the *22IEM03 PriSpecTemp* Project, which was funded by the *European Partnership on Metrology*, the *European Union Horizon Europe Research and Innovation Programme* and by the participating states.

References

1. Gamache, R.R., et al., *Total internal partition sums for the HITRAN2020 database.* Journal of Quantitative Spectroscopy & Radiative Transfer, 2021. **271**.
2. Rothman, L.S., et al., *The HITRAN molecular spectroscopic database and HAWKS (HITRAN Atmospheric Workstation): 1996 edition.* Journal of Quantitative Spectroscopy & Radiative Transfer, 1998. **60**(5): p. 665-710.
3. Yariv, A., *Quantum electronics*. 3rd ed ed. 1989: Wiley.
4. Busch, K.W., et al., *Cavity-ringdown spectroscopy : an ultratrace-absorption measurement technique*. ACS symposium series 720. 1999, Washington, District of Columbia: American Chemical Society.
5. Libbrecht, K.G. and M.W. Libbrecht, *Interferometric measurement of the resonant absorption and refractive index in rubidium gas.* American Journal of Physics, 2006. **74**(12): p. 1055-1060.
6. Cygan, A., et al., *One-dimensional frequency-based spectroscopy.* Optics Express, 2015. **23**(11): p. 14472-14486.
7. Siegel, R. and J.R. Howell, *Thermal radiation heat transfer*. 1981, Washington, D.C: Hemisphese.
8. Ngo, N.H., et al., *An isolated line-shape model to go beyond the Voigt profile in spectroscopic databases and radiative transfer codes.* Journal of Quantitative Spectroscopy & Radiative Transfer, 2013. **129**: p. 89-100.
9. Tennyson, J., et al., *Recommended isolated-line profile for representing high-resolution spectroscopic transitions (IUPAC Technical Report).* Pure and Applied Chemistry, 2014. **86**(12): p. 1931-1943.
10. Birk, M., C. Roeske, and G. Wagner, *High accuracy CO Fourier transform measurements in the range 6000-7000 cm.* Journal of Quantitative Spectroscopy & Radiative Transfer, 2021. **272**.
11. Tran, H., et al., *Non-impact effects in the absorption spectra of HCl diluted in CO, air, and He: Measurements and predictions.* Journal of Chemical Physics, 2023. **158**(18).
12. Reed, Z.D., et al., *SI-traceable molecular transition frequency measurements at the 10^{-12} relative uncertainty level.* Optica, 2020. **7**(9): p. 1209-1220.
13. Cygan, A., et al., *High-accuracy and wide dynamic range frequency-based dispersion spectroscopy in an optical cavity.* Optics Express, 2019. **27**(15): p. 21811-21822.
14. Gordon, I.E., et al., *The HITRAN2020 molecular spectroscopic database.* Journal of Quantitative Spectroscopy & Radiative Transfer, 2022. **277**.
15. Bevington, P.R. and D.K. Robinson, *Data reduction and error analysis for the physical sciences*. 2nd ed. McGraw-Hill international editions: physics series. 1992, New York: McGraw-Hill. xvii, 328 pages : illustrations.
16. Altman, D.G. and J.M. Bland, *Standard deviations and standard errors.* BMJ, 2005. **331**(7521): p. 903.
17. Balashov, A.A., et al., *Measurement and calculation of CO (7-0) overtone line intensities.* J Chem Phys, 2023. **158**(23).
18. Bielska, K., et al., *Subpromille Measurements and Calculations of CO (3-0) Overtone Line Intensities.* Physical Review Letters, 2022. **129**(4).
19. Reed, Z.D., et al., *Effect of Non-Markovian Collisions on Measured Integrated Line Shapes of CO.* Physical Review Letters, 2023. **130**(14).
20. Watson, J.K.G., *Quadratic Herman-Wallis Factors in the Fundamental Bands of Linear-Molecules.* Journal of Molecular Spectroscopy, 1987. **125**(2): p. 428-441.

Supplemental Material for *International Comparison CCQM-P229: Pilot Study to Measure Line Intensities of Selected $^{12}C^{16}O$ Transitions*

1 German Aerospace Center (DLR)

1.1 Description of Experiment

CO measurements were recorded with a Bruker IFS 125 HR Fourier-transform spectroscopy (FTS) spectrometer [21]. A White-type multipass absorption cell with a temperature-controlled cell body and mirrors was used. Details about the set-up can be found in [10] and [22]. Details on common measurement parameters are given in Table 1.1

Table 1.1 Common measurement parameters.

Detector	Room-temperature InGaAs, cut-on 5900 cm^{-1}
Optical filter	Low-pass 7000 cm^{-1}
Source	Tungsten lamp
Beamsplitter	Si on CaF_2
MOPD	100 cm
Input aperture diameter	0.8 mm
Collimator focal length	418 mm
Interferometer pressure	<0.002 hPa (mbar)
Sample	CO 4.7 from Linde company

Spectra of 0.999970 purity CO were taken at ambient temperature. Temperatures were measured with three Pt100 sensors located at the wall of the cell body inside the cell with a standard uncertainty of 0.1 K. Pressures were measured with high-accuracy Mensor or Baratron pressure sensors. The measurement plan was based on the following rationale:

- to measure opaque lines for spectrum zero transmission offset determination
- to operate mostly at pressures >100 hPa => lower relative uncertainty in pressure
- to measure large column amounts for weak lines to compare with NIST, NCU and NIM
- to achieve redundancy by considering multiple sample optical densities
- to measure at 5 hPa, which is Doppler limited and optically thin => optimized for intensities of strong lines
- to determine instrumental line shape for each absorption path using CO_2 measurements at 10 hPa
- use flowing samples for pressures ≤10 hPa, and for those >100 hPa use static samples
- correct for H_2O outgassing by using H_2O partial pressure determined through spectroscopy
- to maintain negligible leak rates

The individual measurement conditions are given in Table 1.2. The pressure range covers 5 hPa to 500 hPa. The root-mean-square noise (RMS) in transmittance ranges from 0.01 % to 0.03 %.

Table 1.2. Measurement conditions.

Molecule	Pressure/hPa	Abs.path/cm	RMS noise/ %
CO	496	1456	0.010
CO	125	1456	0.009
CO	503	5936	0.020

J.T. Hodges et al., 2025 *Metrologia* **62** 08006.
DOI 10.1088/0026-1394/62/1A/08006

CO	257	5936	0.012
CO	126	5936	0.021
CO	5	5936	0.013
CO	502	11696	0.022
CO	250	11696	0.034
CO	117	11696	0.016
CO_2 (ILS)	10	1456	0.010
CO_2 (ILS)	10	5936	0.023
CO_2 (ILS)	10	11696	0.024

1.2 Analysis

For the analysis multispectrum fitting was used as describe in [10], and the Hartmann-Tran line profile [8] with Rosenkranz line mixing was applied. The following list summarizes elements of the analysis.

- Use micro-windows nominally 1 cm^{-1} in width
- For most lines fit the following parameters: S, γ_{0_self}, γ_{2_self}, ν_{VC_self}, δ_{2_self}, Rosenkranz line mixing
- For each micro-window in each spectrum fit a quadratic baseline polynomial, frequency calibration
- Do a zero-transmission baseline offset correction -0.0005 - +0.0005 determined from opaque lines, which however was not available for pathlengths of 14 m and at 5 hPa with a pathlength of 59 m
- Do an absorption path correction for 117 m: on average 0.999
- Do a Van der Waals correction for number density applied (max. 1.00043) – total pressure unchanged
- Omit the 14 m pathlength measurements because of discrepancy with respect to the 5 hPa measurement: residuals up to 0.1% - reason unclear (line model or other explanation)

From coadded residuals we observed an additional line profile contribution at low resolution (±1.5 cm^{-1}) that was not captured by the instrumental line shape fitting software. This profile is antisymmetric with respect to the line center with a maximum amplitude < 0.5 ‰ for an opaque 500 hPa CO line. Implementation of this profile function in the line fitting software did not change the intensities but improved the residuals. An example of the multispectrum fitting is shown in Figure 1.1 Peak-to-peak residuals are mostly < 1 ‰.

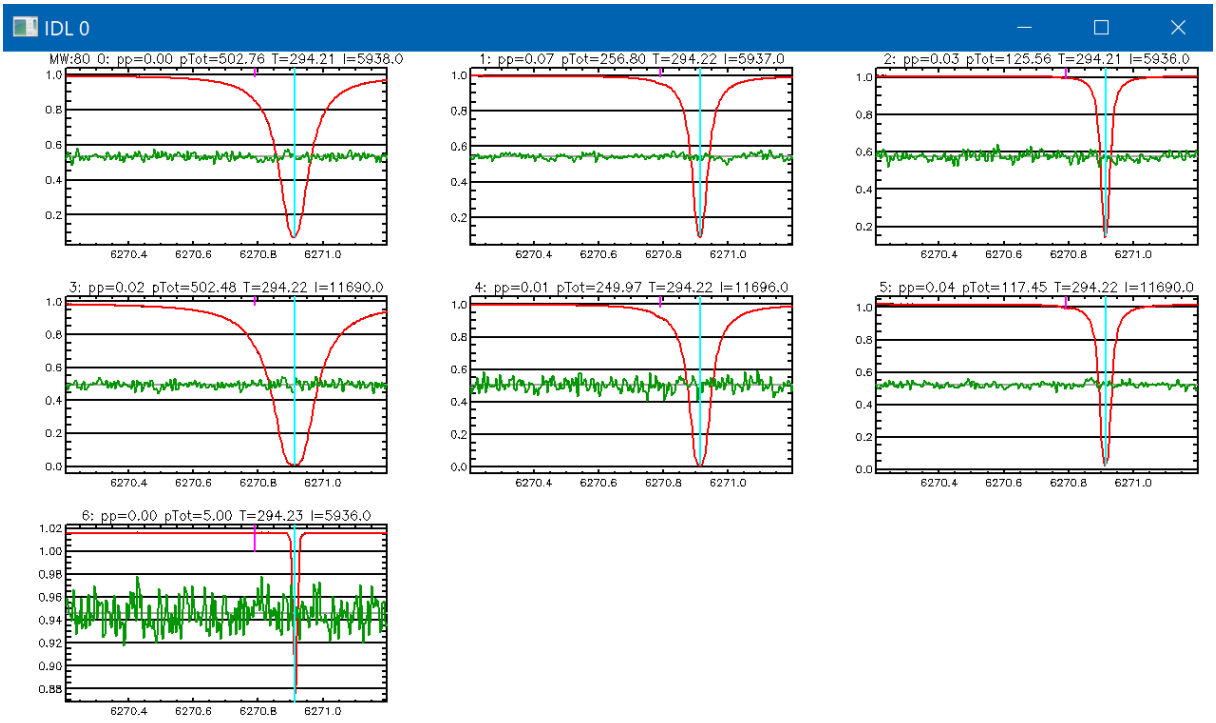

Figure 1.1 Example of multispectrum fit. Black: observed, red: calculated, green: (observed-calculated)×100.

1.3 Uncertainty Analysis

The uncertainty analysis comprises systematic as well as statistical uncertainties. The final relative standard uncertainty values given for the individual lines are the quadrature sum of the individual contributions. Table 1.3 lists the individual systematic error sources, and Table 9.1a gives the relative combined standard uncertainties on a line-by-line basis. They range from 0.81 ‰ to 2.20 ‰, with an average value of 1.01 ‰.

Table 1.3. Systematic line intensity relative standard uncertainty contributions.

Physical Effect	u_r (‰)
Systematic uncertainty in instrumental line shape	negligible
Offset error	0.1
Pathlength	0.2
Molecular lineshape	<0.5
Pressure (drives density)	0.008 >300 hPa 0.2 @ 125 hPa 0.6 @ 5 hPa
Temperature uncertainty 0.1 K	< 0.7 for S >10^{-24} (cm^2 cm^{-1} molec.$^{-1}$) < 2 for S >10^{-25} (cm^2 cm^{-1} molec.$^{-1}$)
Sample purity uncertainty	0.03
Isotopic composition uncertainty (composition determined spectroscopically)	0.12

For validation purposes, we implemented a number density factor analysis. A multispectrum fit was performed fixing the spectroscopic parameters to the results of the previous analysis. For each micro-window in each spectrum a number density factor is fitted. Ideally, these factors should be equal to 1. Differences from unity reveal systematic error sources and may be used to qualify the uncertainty analysis. Figure 1.2 shows the number density factors in the different spectra vs. line intensity. Large opacities > 4 should not be considered because the number density factor become very sensitive to systematic errors. On average, the number density factors differ from 1 by less than 0.5 ‰, which is well within the total uncertainty budget.

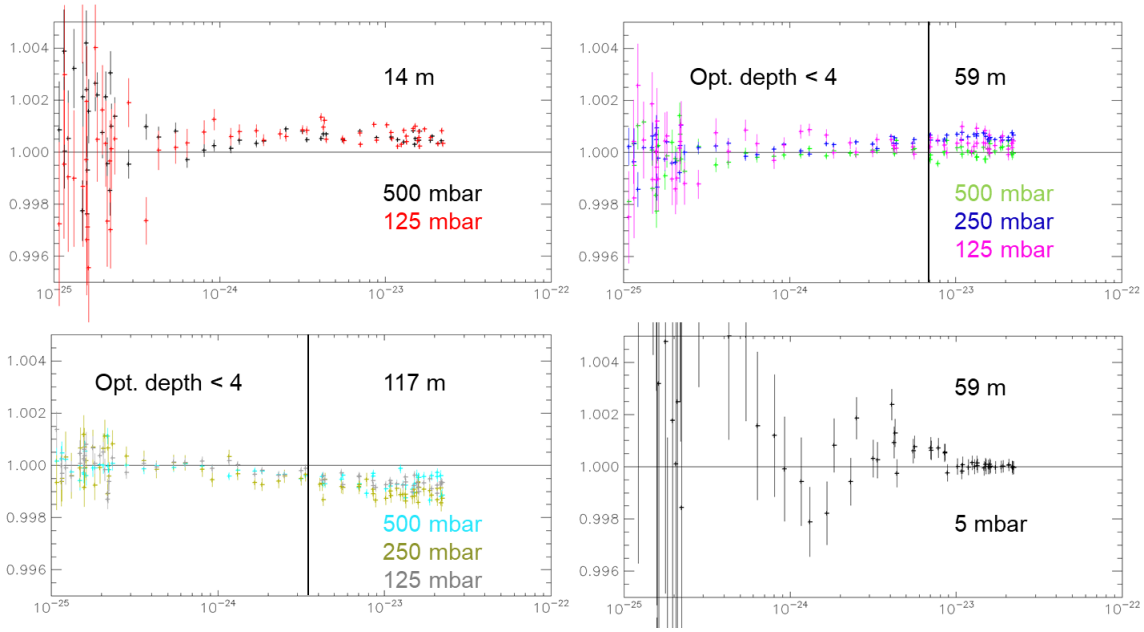

Figure 1.2. Number density fits for all spectra and all micro-windows. The line intensity refers to the strongest line in each micro-window.

1.4 Determination of optical pathlength

As described in Birk et al, [10], the spectrometer was equipped with a multi-pass cell of base length 0.8 m and adjustable folding mirrors giving pathlengths that were adjustable in increments of 6.4 m over the range 15 m to 207 m. In the present study, three pathlengths of approximately 15 m, 60 m and 117 m were used. These distances were accurately determined with relative standard uncertainties of 1 ‰ from mechanical measurements and tolerances of the assembly. Ray tracing analysis of the divergence of marginal rays was used to correct these path lengths by 0.81 ‰ for the shortest path and 0.20 ‰ for the two longer paths. These corrections resulted in pathlengths of 14.56 m, 59.36 m and 116.96 m, with all three cases having relative standard uncertainties of 0.2 ‰.

1.5 Determination of $^{12}C^{16}O$ isotopologue abundance

The relative abundances, χ_i, of the four most abundant stable CO isotopologues $^{12}C^{16}O$ (26), $^{13}C^{16}O$ (36), $^{12}C^{18}O$ (28), and $^{12}C^{17}O$ (27) in the sample gas were determined spectroscopically from peak area ratios in the 3-0 band. The two least abundant isotopologues, $^{13}C^{18}O$ (38), $^{13}C^{17}O$ (37) were assumed to occur at the HITRAN 2020 [14] abundances. The set of χ_i was calculated from these measurements assuming a stochastic distribution of C and O isotopes combined with HITRAN 2020 [14] line intensities. These measurements indicate that the sample was enriched in $^{12}C^{16}O$ by 0.30 ‰ compared to the HITRAN value

of 0.98544 for this isotopologue. We also note that the $^{12}C^{18}O$ isotopologue was enriched by 32 ‰ relative to the corresponding HITRAN value. See Table 6.2 for a summary of these results.

Table 1.4 Summary of CO isotopologue abundance results

isotopologue	26	36	28	27	38	37
χ_{HITRAN}	0.986544	0.011084	0.001978	3.6787E-4	2.2225E-5	4.1329E-6
$\chi_{meas}/\chi_{HITRAN}$	1.000303	0.9655979	1.0321338	1.0522045	1	1
χ_{meas}	0.986843	0.01070269	0.0020416	3.8707E-4	2.2225E-5	4.1329E-6

1.6 Outlook

The analysis did not account for intensity depletion, which redistributes intensity from the line core to the far wings. This effect can be explained in terms of the breakdown of the impact approximation (assumed for standard line profiles such as the HTP) whereby the duration of collisions is assumed to be instantaneous. The analysis could be refined by accounting for this effect, which varies with rotational quantum number and pressure. Furthermore, instead of the van der Waals correction the more advanced Soave-Redlich-Kwong equation should be used. It would be more appropriate to use the correction on the total pressure instead of the absorption path as discussed in [22].

2 Korea Research Institute of Standards and Science (KRISS)

2.1 Description of Experiment

A schematic of the cavity ring-down spectroscopy (CRDS) spectrometer used in this intercomparison is depicted in Fig 2.1. The system includes both a laser frequency stabilization subsystem and a length tunable ring-down cavity. The external cavity diode laser (ECDL) (TOPTICA, CTL 1550) was locked to an optical frequency comb (OFC) (f_{rep}=250 MHz, f_{ceo} = 20 MHz, Menlo), of which the repetition rate and the carrier envelope offset frequency were locked to a GPS-referenced Cs clock (10 MHz, SRS, FS740). For optical beat signal detection, the ECDL and the filtered OFC beams were coaxially propagated and focused onto an InGaAs detector (400 MHz, Thorlabs, APD430C/M), and the OFC out-of-band wavelengths were filtered by fiber Bragg gratings (FBGs) centered at the wavelengths of the measurand lines. The measured beat frequency between the ECDL and OFC was actively locked to a 62.5 MHz radiofrequency local oscillator (LO). The cavity mode frequency was scanned across the stabilized ECDL frequency by actuating one cavity mirror with a tubular PZT. The ECDL was relocked to the OFC when its frequency reached the neighboring comb mode. The comb mode at the starting point of the scanning was checked by the wavelength meter (uncertainty ~ 60 MHz, High Finesse, WS7-60). Therefore, the optical frequency scanning distance was added by $n \cdot f_{rep}/2$ at every relock point.

The ring-down cavity consisted of two high-reflectivity mirrors (R > 99.997 % at 1559.9 nm, radius of curvature of 1 m), separated by 18.55 cm giving a free spectral range of 810 MHz. Matching of the laser transverse spatial profile to the TEM_{00} optical cavity mode was realized using a single focusing lens. One mirror was attached to the PZT for displacement, and the length of the optical cavity was repeatedly modulated at 60 Hz to periodically generate build-up of laser light into a single longitudinal mode of the ring-down cavity. The entire cavity assembly was in a rectangular enclosure of dimensions (36.5 cm ×15 cm × 16.5 cm).

After buildup the intra-cavity power was extinguished using an optical switch (OSW, Epiphotonics, PLZT) having a rise time less than 10 ns with an extinction ratio of 30 dB. The OSW was

triggered by a TTL pulse which was generated by the delay generator (DG, Stanford Research System, DG535) which was in turn triggered when the PD signal level exceeded a specified threshold. Each ring-down trace was recorded by an oscilloscope (400 MHz, 14 bit, 1 GS/s, National Instrument, PXIe-5164) synchronized to the DG. Although the OSW did not completely extinguish the laser transmission because of its low extinction ratio, decay signals were generated as the moving mirror swept the cavity resonance through the laser frequency. We note that typically, ring-down spectrometers using continuous wave lasers incorporate acousto-optic or electro-optic modulators (> 50 db extinction ratio) to extinguish the probe laser beam. For these reasons, we speculate that the excess scatter exhibited by the KRISS line intensity data (by comparison to the other five laboratories in the present study and rendering these data as outliers) was caused by the low extinction ratio of the optical switch. Unfortunately, this limitation was not identified in time to meet the final deadline of this intercomparison.

The amount of gas in the CRDS cell (flow configuration) was controlled at constant pressure using a pressure controller (WIKA, CPC6050). The cell pressure was measured using a capacitance diaphragm gauge (MKS, 690A12TRA), which was calibrated by the KRISS primary standard (capacitance diaphragm gauge, calibrated in 1-100 Torr). The cell temperature was not controlled but was measured with a platinum resistance thermometer sensor (FLUKE, 5628), which was traceable to NIST temperature standards.

Intensities of the R23, P22, R25, and R28 transitions of $^{12}C^{16}O$ were determined in terms of the measured spectroscopic peak areas. Each absorption spectrum was centered on the transition with a halfwidth of 6.25 GHz. The average ring-down signal at each optical frequency was based on 1000 decays. The peak areas of individual spectra were averaged over 27, 18, 20, and 13 spectra, respectively. Optical frequency scanning and ring-down signal acquisition was controlled using in-house Labview code, and CRDS spectra were constructed by custom Matlab code.

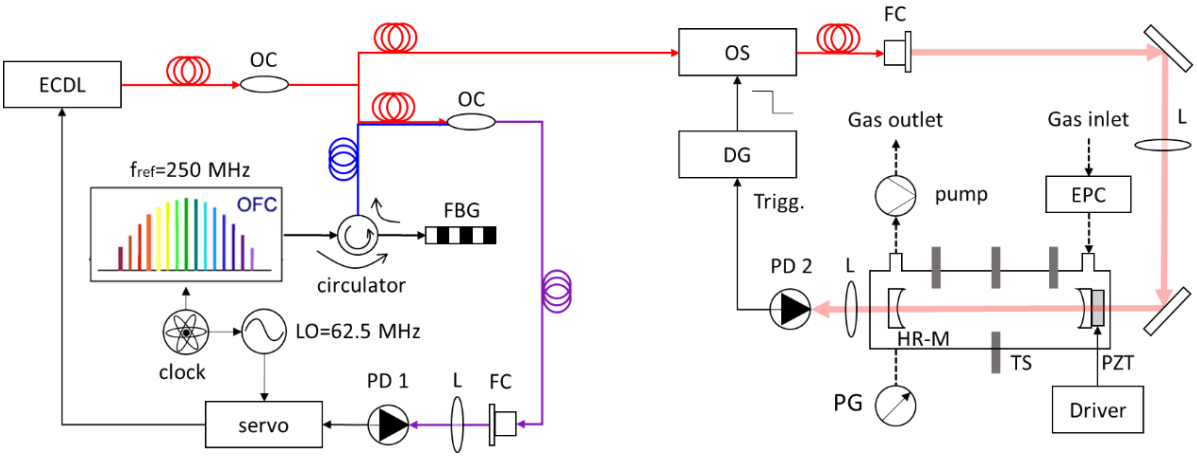

Fig 2.1. Layout of comb-locked CRDS serving CCQM-P229. OC: optical coupler, L: lens, PD: photo detector, OFC: optical frequency comb, FBG: fiber brags grating, LO: local oscillator, PZT: piezo electric transducer, OS: Optical switch, DG: Delay generator, PG: Pressure gauge

2.2 Data analysis

Each reported average line intensity and its uncertainty was based on the respective sets of measured spectra. These intensities were normalized to 296 K using the Excel sheet provided by the coordinating lab. An overview of the data analysis procedure is depicted in Fig. 2.2.

Submeasurement No.	Peak area	Line intensity at 296 K
1	a_1 (T_1, P_1, n_1)	$S_{0,1}$
2	a_2 (T_2, P_2, n_2)	$S_{0,2}$
3	a_3 (T_3, P_3, n_3)	$S_{0,3}$
4	a_{41} (T_4, P_4, n_4)	$S_{0,4}$
…	…	…
N	a_N (T_N, P_N, n_N)	$S_{0,N}$
Final line strength, $S_0 = \frac{\sum_{i=1}^{N} S_{0,i}}{N}$		

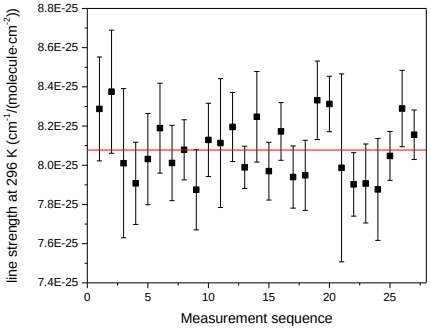

Figure 2.2. Uncertainty evaluation method for reporting line strength value and associated uncertainty.

The area of the measured absorption line was derived after optimal fitting using the Hartmann-Tran profile [8]. The absorption coefficient was derived according to following equation.

$$\alpha(\nu) = \frac{1}{c}\left(\frac{1}{\tau(\nu)} - \frac{1}{\tau_0(\nu)}\right), \tag{2.1}$$

where α is absorption coefficient, c is speed of light, τ and τ_0 are the decay times with sample absorption and in the spectrum baseline, and ν is wavenumber.

2.3 Uncertainty Analysis

The uncertainties of the measurement parameters affecting the line intensity were linearly propagated through the model equation as in the Excel file. The GUM workbench was used to compute the uncertainty of the resulting intensities. As an example, Table 2.1 highlights the uncertainty of the thirteenth measurement of the R23 line. Temperature, and pressure were observed as a function of time, to show random variations as depicted in Fig 2.2.

Table 2.2 Uncertainty budget for thirteenth sub measurement of R23 ($S_{0,13}$ of R23)

Type of Uncertainty	Component	Value	Relative expanded uncertainty (%)	Relative Contribution to the uncertainty of the line strength (%)
Type A	Temperature, T (K)	296.47	0.020	0.0
	Pressure, P (kPa)	1.901	0.003	0.0
	Peak area, a_{line} (cm^{-2})	3.6423×10^{-7}	6.998	62.4
Type B	Amount fraction, x_{co} (mol/mol)	0.99998	0.000	0.0
	Partition sum, Q_T	107.590	0.003	0.0
	Isotope ratio, r_{iso}	0.98654	0.040	37.6
Constant	k=1.3806e-23 J/K, Q_{T0}=107.419, h=6.6260e-34 J/Hz, c=299792458 m/s, E"=1059.3718 cm^{-1}, T_0=296K			

DOI 10.1088/0026-1394/62/1A/08006

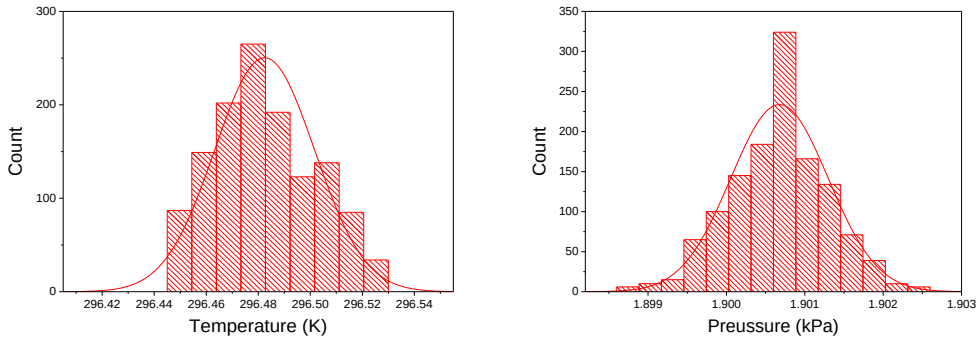

Figure 2.3. Histograms of temperature (left) and pressure (right) variations for all R23 intensity measurements.

There was no evidence of correlation between the temperature and pressure. In the case of peak area, its uncertainty was estimated in terms of the standard deviation of the fit residuals according to

$$u(A_{line}) = \sqrt{\frac{\sum_{i=1}^{N}(\alpha(\nu_i)-\alpha_{fit}(\nu_i))^2}{N-1}}, \quad (2.2)$$

where α and α_{fit} are the measured absorption coefficient and the fitted absorption coefficient at i^{th} wavenumber bin, respectively, and N is the total number of frequency bins. The uncertainty of the amount fraction of CO was taken from the purity certification of the gas provider. Because the partition function is a temperature dependent function, its contribution to the uncertainty was accounted by the temperature variation. We assumed the relative abundance of the $^{12}C^{16}O$ isotopologue was set by the HITRAN 2020 value for this species, χ_{26} = 0.986544 [14].

Table 3.2. Summary of line intensity measurements of $^{12}C^{16}O$.

Rot quant # J	Wavenumber (cm^{-1})	Wavelength (nm)	Number of measurements	P_{avg} (kPa)	T_{avg} (K)	Temperature-corrected intensity ($cm^2cm^{-1}molec.^{-1}$)
R23	6410.88	1559.848	27	1.901	296.49	$(8.0182\pm0.044) \times 10^{-25}$
P22	6241.85	1602.089	18	1.948	296.49	$(6.5587\pm0.178) \times 10^{-25}$
R25	6413.12	1559.303	20	1.901	296.54	$(3.4780 \pm0.038) \times 10^{-25}$
R28	6415.67	1558.684	13	5.970	296.49	$(9.337\pm0.132) \times 10^{-26}$

3 Nicolaus Copernicus University (NCU)

3.1 Description of Experiment

Measurements at NCU were performed with the cavity mode-dispersion spectroscopy (CMDS) technique [6], which is based on measurements of frequencies of the high-finesse optical cavity resonances, shifted due to a resonant dispersion. In the presence of resonant absorption α_q corresponding to the q^{th} cavity mode of frequency ν_q, a resonance-induced dispersion in line center is also observed. The absorption and dispersion are related to real and imaginary part of the resonant refractive index, respectively:

$$n(\nu_q) = n_0 + n'(\nu_q) - i\kappa(\nu_q). \quad (3.1)$$

Here n_0 is the non-resonant refractive index. The absorption causes broadening of the cavity mode width (HWHM) by $\Delta\Gamma_q$, whereas the dispersion causes the mode frequency to shift by $\Delta\nu_{D,q}$. The cavity mode broadening is related to the absorption coefficient by the following relation:

$$\alpha_q = \frac{4\pi}{c}\Delta\Gamma_q \,, \tag{3.2}$$

where c is the speed of light. The dispersive shift of the q^{th} cavity mode is related to its broadening by the relation [23]

$$\frac{\Delta\nu_{D,q}}{\Delta\Gamma_q} = -\frac{n\prime(\nu_q)}{n_0\kappa(\nu_q)} = \frac{\Phi_I(\nu_q-\nu_{\eta\eta\prime})}{n_0\Phi_R(\nu_q-\nu_{\eta\eta\prime})} \tag{3.3}$$

where $\Phi_I(\nu_q - \nu_{\eta\eta\prime})$ and $\Phi_R(\nu_q - \nu_{\eta\eta\prime})$ are the imaginary and real parts of the complex line shape function of the transition under investigation, respectively, and $\nu_{\eta\eta\prime}$ is the transition frequency. Using the above relations, one obtains the relationship between the dispersive mode shift, $\Delta\nu_D$, line intensity, S, absorber concentration n_a, and the line-shape function, Φ, given by Eq. (10) of the present Final Report Summary document.

We have shown that the CMDS technique, relying on determination of cavity mode-shifts due to resonant dispersion, leads in our system to more accurate results [13] than the more commonly used cavity ring-down spectroscopy (CRDS) and recently developed cavity mode-width spectroscopy techniques [13, 24]. The experimental setup and the principle of its operation are as in Ref. [13]. The absorption cell is a high-finesse, 73 cm-long optical cavity formed with two spherical mirrors in a non-confocal configuration having an internal volume of approximately 0.2 l. The intensity reflectivity, *R*, of the cavity mirrors is nominally $R = 0.999923$ at the probe wavelength range near 1.6 μm, corresponding to transitions under investigation, and $R = 0.98$ for wavelength of 1.064 μm, corresponding to the frequency-stabilized Nd:YAG laser used for stabilization of the cavity length. The probe laser frequency is locked with the Pound-Drever-Hall (PDH) technique to a cavity mode located in a low absorption region, several GHz from the transition under investigation. Part of the probe laser beam, serving as the probe beam, has a polarization orthogonal to the lock beam. It is frequency-detuned with an acousto-optic modulator (AOM) and scanned over consecutive cavity modes with a sideband generated by an electro-optic modulator (EOM) having the frequency tuning range of nearly 20 GHz. The mode positions are determined with Hz-level uncertainty relative to the frequency of the selected mode which is locked. The spectrum frequency axes were referenced to a UTC(AOS) frequency reference via an optical frequency comb (OFC) for all lines except for the P20 and P22 lines. The UTC(AOS) reference was provided via the OPTIME network [25]. Its relative stability is 10^{-12} at 1 s and is realized by a hydrogen maser. For lines P20 and P22 only the relative frequency axis is linked to UTC(AOS) by referencing all RF signals to the 10 MHz RF signal delivered by the OPTIME network.

The temperature of the optical cavity was actively stabilized at 296 K with four Peltier elements working in a heating or cooling regime, as necessary. The temperature gradient along the cavity long axis was adjusted with two additional heaters and reduced to less than 50 mK. Altogether, the temperature was stabilized at 296.00(3) K. As a sample we used a commercial CO sample from Linde Gas near natural isotopic abundance and stated purity of 0.99997. Sample pressure was measured with a Wika/Mensor CPG2500 gauge having a full-scale range of 120 kPa and nominal relative standard uncertainty of 0.08 ‰ for the set of five weaker lines, and with MKS Baratron 690 A capacitance diaphragm gauge having a full-scale range of 10 Torr and nominal relative standard uncertainty of 0.5 ‰ for the stronger lines.

3.2 Measurements and Data Analysis

We measured intensities of 10 lines from CO (3-0) band. For each line, measurements were done at three to five pressures, see Table 3.1. The spectra were fitted with Hartmann-Tran profile (HTP) [8] with incorporated first-order line-mixing or its simplification, the speed-dependent hard collision profile (SDHCP), which is also called the speed-dependent Nelkin Ghatak profile (SDNGP). For fitting we used a multi-spectrum fit approach for collisional broadening, shifting, frequency of velocity changing collisions, speed-dependence parameters of broadening and shift, as well as for the unperturbed transition frequency. The fit quality (QF) varies between 19000 and 75000 and is given in Table 3.1. The line area was fitted independently at each pressure and the line intensity was determined from a linear fit to the dependency of the line area with pressure. Figure 3.1 shows measured spectra together with the fit residuals for the R7 line.

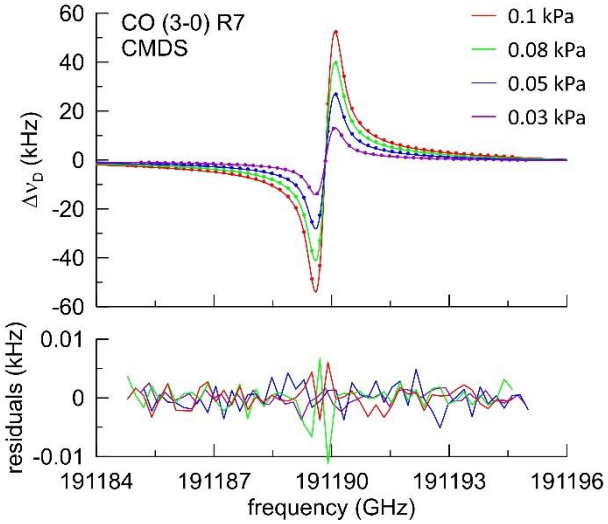

Figure 3.1. $^{12}C^{16}O$ (3-0) line R7 measured at NCU. Top panel: spectra measured (points) and fitted with HTP (lines) for four measurement pressures indicated with different colors. Bottom panel: residuals (measured-fitted) from the multispectrum fit of the R7 line.

Table 3.1. Measured lines, minimal and maximal measurement pressure, $p_{\min}$ and $p_{\max}$, respectively, number of pressures measured and quality-of-the-fit (QF) for each line.

Line	$p_{\min}$ (kPa)	$p_{\max}$ (kPa)	no. of pressures	QF
P22	1.6	6.4	4	23000
P20	0.8	3	3	41000
P16	0.3	0.8	3	75000
P10	0.2	0.4	3	43000
P1	0.3	0.8	3	48000
R7	0.03	0.1	4	47000
R16	0.1	0.3	3	38000
R23	0.7	2	3	32000
R25	1.3	7	5	30000
R28	3	20	5	19000

3.3 Uncertainty Analysis

The line intensity is determined in our experiment from the formula:

$$S(T_{\mathrm{ref}}) = kTf_S(T)a_{p\prime}f_{p\prime} \tag{3.4}$$

Here $S(T_{\mathrm{ref}})$ is the line intensity determined at reference temperature T_{ref} = 296 K, k is the Boltzmann constant, T is the temperature of measurement, $f_S(T) = S(T_{\mathrm{ref}})/S(T)$ approximates the temperature dependence of the line intensity (taken from HITRAN), $a_{p\prime}$ is the coefficient resulting from the linear fit of the line areas versus pressure indicated by pressure sensor, p', and $f_{p\prime} = p'/p$ is the ratio of measured pressure and the true sample pressure. As the cavity temperature was stabilized at T_{ref}, we assume that $f_S(T) = 1$ and $f_{p\prime} = 1$. However, both these quantities have non-zero uncertainty: f_S due to uncertainty of the temperature measurement and the temperature gradient along the cavity, whereas $f_{p\prime}$ due to uncertainty of the pressure calibration, sample impurity, sample isotopic composition and real gas approximation.

Two of the quantities on the right side of Eq. (3.4), namely T and $f_S(T)$, are not independent. The correlation between them may increase or decrease the total uncertainty of the line intensity, thus a proper correlation component needs to be included. Consequently, the relative uncertainty of the line intensity, $u(S)/S$, may be given in a similar form as in Ref. [26]:

$$\frac{u(S)}{S} = \sqrt{\left[\frac{1}{T^2} + \frac{1}{f_S^2}\left(\frac{\partial f_S}{\partial T}\right)^2 + 2\frac{1}{Tf_S}\frac{\partial f_S}{\partial T}\right]u^2(T) + \frac{u^2(a_{p\prime})}{a_{p\prime}^2} + \frac{u^2(f_{p\prime})}{f_{p\prime}^2}} \quad . \tag{3.5}$$

Contributions to the line intensity uncertainty are listed in Table 3.2.

Table 3.2**.** Contributions to the total uncertainty of the determined line intensities. All uncertainty values are given as standard uncertainty (1σ). All components, apart from those in the first row, are given as relative values.

component	value	subcomponent	value
$u(T)$	30 mK	$(\partial f_S/\partial T)/f_S$	-0.019 K^{-1} to + 0.0033 K^{-1}
$u(a_{p\prime})/a_{p\prime}$	0.0006 to 0.00072	fit uncertainty	0.000037 to 0.00038
		spectrum modelling	0.0006
$u(f_{p\prime})/f_{p\prime}$	0.00042 to 0.0008	pressure sensor calibration	0.00012 to 0.0007
		sample purity	0.00003
		sample isotopic composition	0.00012
		real gas correction	not exceeding 0.000072
$u(S)/S$ (‰)	**0.83 to 1.1**		

DOI 10.1088/0026-1394/62/1A/08006

3.4 Isotopic analysis

The $^{12}C^{16}O$ (26) abundance, χ_{26}, was determined by spectroscopically by measuring peak areas, a, for the pair of R7 ($^{13}C^{16}O$) and R23 ($^{12}C^{16}O$) 3-0 band transitions. This choice of probed lines and subsequent analysis is the same as that given below in Sec. 5.3 where the isotopic determination of the NIST samples was described. The measured area ratio was $a(^{12}C^{16}O)_{R23}/a(^{13}C^{16}O)_{R7}$ = 3.8714(46) at T = 296 K, yielding $\delta^{13}C$ = –60.4 ‰ and χ_{26} = 0.987257 with a standard relative uncertainty of 0.12 ‰. This measured relative abundance corresponds to an enrichment of 0.72 ‰ with respect to the HITRAN 2020 value of 0.986544 [14].

4 National Institute of Metrology (NIM)

4.1 Description of Experiment

The spectra were measured using the custom, comb-assisted, length-stabilized cavity ring-down spectrometer at the National Institute of Metrology [27]. For this setup, the cavity length was stabilized against a frequency-stabilized HeNe laser, and the probe laser frequency was actively locked to the ring-down cavity using the Pound-Drever-Hall (PDH) technique. The two-mirror cavity was nominally 1 m long with finesse of 1.9×10^5. A Mach-Zehnder modulator was used to step the probing frequency using radio-frequency sidebands. A wavelength meter and a Rb-clock-referenced optical comb were used to measure the absolute frequency of the probe laser and provide an accurate measure of the spectrum detuning axis. The cavity temperature was precisely controlled to assure that all the data were acquired between 295.99 K and 296.01 K. Four pressure gauges with full-scale ranges of (13.3 Pa, 133 Pa, 1.33 kPa, 13.3 kPa) were used to measure sample pressure.

For each transition, a set of 9 spectra were measured at different pressures. Data analysis involved fitting a speed-dependent Nelkin Ghatak profile (SDNGP) to the measured spectra using a multi-spectrum least-squares fitting method.

Table 4.1 Summary of uncertainty contributions for the measurements made by NIM. All values are relative standard uncertainties in ‰.

	P 1	P 10	P 16	P 20	P 22	R 7	R 16	R 23	R 25	R 28
Type A										
Multi-spectrum fit	0.32	0.24	0.39	0.43	0.25	0.28	0.18	0.19	0.36	0.30
Peak area vs. p fit	0.78	0.24	0.63	0.53	0.58	0.27	0.31	0.21	1.36	0.83
Reproducibility	2.1	2.1	2.1	2.1	2.1	2.1	2.1	2.1	2.1	2.1
Type B										
Rb clock accuracy	3.E-08	3.E-08	3.E-08	3.E-08	3.E-08	3.E-08	3.E-08	3.E-08	3.E-08	3.E-08
Rb clock aging	3.E-07	3.E-07	3.E-07	3.E-07	3.E-07	3.E-07	3.E-07	3.E-07	3.E-07	3.E-07
Cavity instability	3.E-07	3.E-07	3.E-07	3.E-07	3.E-07	3.E-07	3.E-07	3.E-07	3.E-07	3.E-07
PDH locking	1.E-09	1.E-09	1.E-09	1.E-09	1.E-09	1.E-09	1.E-09	1.E-09	1.E-09	1.E-09
FSR measurement	3.E-11	3.E-11	3.E-11	3.E-11	3.E-11	3.E-11	3.E-11	3.E-11	3.E-11	3.E-11
P	0.80	1.85	1.25	0.40	0.30	1.85	1.85	0.30	0.20	0.20
T	0.05	0.05	0.05	0.05	0.05	0.05	0.05	0.05	0.05	0.05
CO Purity	0.00	0.00	0.00	0.00	0.00	0.00	0.00	0.00	0.00	0.00
Isotopic composition	0.01	0.01	0.01	0.01	0.01	0.01	0.01	0.01	0.01	0.01
Combined	2.40	2.82	2.55	2.24	2.21	2.83	2.82	2.14	2.53	2.29

To evaluate uncertainty, we used a similar method to that described in our recently published work on CO_2 line shape parameters [28]. Here we found that statistical (type A) uncertainties were dominated by three components: 1) uncertainty from the multi-spectrum fitting, 2) uncertainty from fitting peak area vs. pressure, and 3) an unidentified source of measurement reproducibility. This third component was first noticed upon the doing the integrated analysis of the results presented in the Final Report Summary. By comparison to the intensity data from all other laboratories considered (*i.e*. DLR, NIM, NCU, NIST, PTB), the average of the NIM data was consistent with the weighted-mean intensity over all these laboratories. However, the NIM data exhibited an excess scatter of about 2.1 ‰ about this weighted-mean value which far exceeded the combined Type A uncertainties from multispectrum fitting of the spectra and from fits of peak-area vs. pressure. This excess scatter was ascribed to an unidentified irreproducibility in the measured intensities that could not be captured by these components in Table 4.1.

Systematic (type B) source of uncertainty included accuracy and aging of the 10 MHz Rb oscillator to which the optical frequency comb was referenced, instability in the cavity length, PDH locking, determination of the cavity free spectral range (FSR), measured pressure, *p* and temperature *T*, CO purity and isotopic relative abundance. We found that contributions from the Rb clock, cavity instability, PDH locking and uncertainty in FSR measurement were negligible. Rather our primary sources of uncertainty are related to fitting the measured line shapes, measurement of sample pressure and irreproducibility in the measured spectra. A detailed list of the considered sources is given below in Table 4.1.

4.2 Determination of $^{12}C^{16}O$ relative abundance

The isotope ratio, $^{13}C/^{12}C$, of the CO sample was measured using mass spectrometry by the Division of Chemical Metrology and Analysis Science at NIM. This measurement was referenced to the Vienna Pee Dee Belemnite (VPDB) scale using the reference ratio $^{13}R = 0.011180$ [29] giving $\delta^{13}C_{VPDB} = -20.646$ ‰ ± 0.48 ‰. For the oxygen isotopes, the relative abundance of ^{16}O was calculated to be 0.997525, using the VPDB reference isotope ratios for ^{17}O and ^{18}O given by $^{17}R = 0.0003931$ and $^{18}R = 0.00208835$, respectively [30]. Assuming a stochastic distribution of C and O isotopes the relative abundance of the $^{12}C^{16}O$ isotopologue was determined to be 0.9867209 with a relative standard uncertainty of 0.01 ‰.

5 National Institute of Standards and Technology (NIST)

5.1 Description of Experiment

All spectra were acquired using a cavity ring-down spectrometer which was actively locked to an optical-frequency-comb (OFC) as discussed in [12, 18, 19]. Here the reference to the optical frequency comb (OFC) was the 10 MHz output of Rb clock, rather than the Cs clock used in these prior studies. This slight modification in the OFC reference did not contribute significant additional uncertainty to the spectrum area measurements. The spectrometer comprised an optical cavity with two mirrors (intensity reflectivity R = 0.99997 in the spectral region considered here) separated by 139 cm. One cavity mirror was attached to a piezo-electric transducer (PZT) to allow for fine tuning the cavity resonance frequencies. The probe beam originated from an external cavity diode laser (ECDL) emitting a tuneable single-frequency laser beam that was subsequently amplified by a fiber amplifier, modulated by a switchable, radio-frequency (RF)-electro-optic phase modulator (EOM) yielding RF tuneable optical sidebands which could be rapidly extinguished (80 dB extinction ratio) to initiate ring-down decay events. The carrier frequency of the ECDL (as well as the EOM sidebands) was actively stabilized with respect to a tooth of the OFC using phase-sensitive detection between a local oscillator (60 MHz) and the heterodyne beat signal obtained by combining the OFC and probe laser beams. To close the servo loop, this error signal was fed back through a proportional-integral (PI) loop filter to drive electrical current on the ECDL. In addition, active stabilization of the cavity length with respect to a stabilized sideband of the EOM was achieved by periodically sweeping the cavity length using the PZT-actuated ring-down mirror. A low-bandwidth PI servo (10 Hz) feeding back to the cavity length adjustment enabled locking the average cavity mode frequency at each spectral position with

a precision better than 1 kHz as described in [12]. Individual spectra were acquired by scanning one of the optical sidebands of the EOM through multiples of the cavity free spectral range (~110 MHz) and acquiring 100 decay signals per spectrum point.

Ring-down signals were acquired using a reference-grade digitizer as described in [31]. Allan deviation analysis exhibited a single-wavelength noise-equivalent absorption coefficient for time scales up to 60 s of 8×10^{-12} cm^{-1} $Hz^{-1/2}$, whereas the empty-cavity root-mean-square spectrum showed a baseline noise of 1.4×10^{-11} cm^{-1} which was limited by residual etalon effects. All spectra were acquired on static samples at 296 K ± 0.02 K, with the cell temperature measured using a NIST-calibrated platinum resistance thermometer (PRT) making good thermal contact with the cell walls.

The pressures of the CO samples ranged from 3 Pa to 830 Pa and were measured with one of two temperature-regulated capacitance diaphragm gauges (133 Pa and 1.33 kPa full-scale ranges). Each gauge was an accurate secondary transfer standard that was directly calibrated against a primary pressure standard at NIST [32].

The relatively low pressures considered here demanded that we pay special attention to minimize potential confounding effects such as leaks of ambient air into the system, gas desorption from walls, incomplete pumping of the sample from previous fill cycles, and variations in the pressure gauge zero. The sequence of steps involved is summarized in Table 5.1 with reference to the corresponding experimental layout shown in Fig. 5.1. This systematic approach for introducing and removing the gas samples was designed to minimize uncertainty in the measured CO pressure. A complete measurement cycle involved the four

Table 5.1. Sequence of steps involved in a fill and pump cycle for introducing and removing static charges of CO as depicted in Fig. 5.1. Here $V_1 - V_4$ correspond to the valves indicated in Fig. 5.1, where (O) and (C), indicate the valve status, which was either open or closed. The last column indicates the nominal duration of each step.

step	**operation**	**V1**	**V2**	**V3**	**V4**	**Δt**
1	zero pressure gauge	O	C	C	C	15 h
2	introduce sample (fill)	C	O	C	O	< 1 min
3	measure p and $\alpha(\nu)$	C	O	C	C	5 – 10 min
4	remove sample (pump out)	C	O	O	C	0.5 h

steps given in Table 5.1. Importantly, we note that the pressure gauge transfer standards were differential devices. At the beginning of the cycle (step 1) both the reference and measurement sides of the chosen pressure standard were evacuated to 2×10^{-3} Pa using an ion pump. In step 2, the measurement side of this gauge was isolated from the ion pump, and the evacuated sample volume (ring-down cell plus measurements side of the pressure gauge) was briefly charged with source gas by opening V4. Next, the spectrum measurement time interval (step 3), was initiated by closing V4. Typically, three to five spectra were acquired for each fill of the sample volume. Subsequently, V3 was opened for an extended time to allow the turbo pump to remove the sample and begin step 4. Note that it was necessary to zero each pressure gauge only once per day (step 1) after pumping on the two ports overnight because this result was stable over the course of a day.

The last pumping operation (step 4) typically took about 0.5 h. This evacuation time resulted in a baseline pressure of ~0.01 Pa, which was limited by leakage of air into the system. Importantly, we performed spectroscopic peak area measurements of the R7 3-0 band of $^{12}C^{16}O$ line to accurately estimate the amount of residual CO remaining from the previous fill cycle. After having pumped out the charge (end of step 4), this measurement typically yielded a CO partial pressure of about 5×10^{-4} Pa, with the remainder of the residual charge assumed to be air. Moreover, after isolation of the sample volume and prior to introducing the next charge of CO, a steady linear increase of pressure with time (nominally 2×10^{-4} Pa min^{-1}) caused by leakage of ambient air into the system was also monitored. This pressure was recorded and provided enough

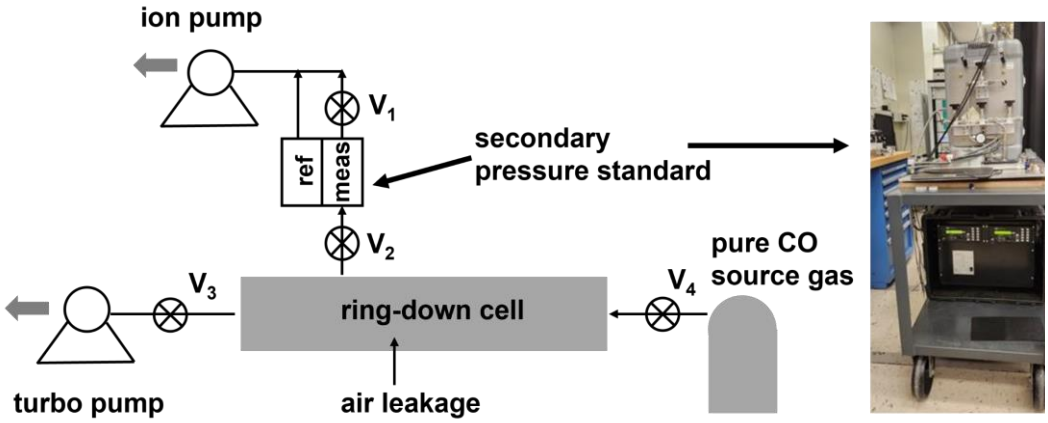

Figure 5.1. Setup for minimizing uncertainty measuring the pressure of static CO samples. The secondary pressure standard (photograph on the right side) comprises two temperature-regulated, differential capacitance diaphragm gauges (each with reference and measurement ports) calibrated with respect to a NIST primary standard manometer. The state (open, closed) of each isolation valve, V_i (i: 1 – 4), during each step of the fill and pump cycle is given in Table 5.1.

information to account for the time-dependent dilution (by ambient air) of the CO sample which must have occurred during the subsequent spectrum acquisition. After introduction of the CO charge (step 2), we found no evidence of sample adsorption on the cell wells, although the pressure measurement took about 1 min to stabilize because of transient mass transfer of the charge within the entire sample volume. As discussed below, this finite response rate introduced a small uncertainty on our ability to estimate the CO partial pressure at $t = 0$ (corresponding to the closing of V4 at the end of step 2).early annual calibration of the NIST transfer stand for pressure results in a system with the uncertainties shown in Fig. 5.2. Except for the lowest pressure considered here (3 Pa), the relative standard uncertaintyis less than 1 ‰ and falls off with closely with the square root of pressure up to 1000 Pa and beyond. Because

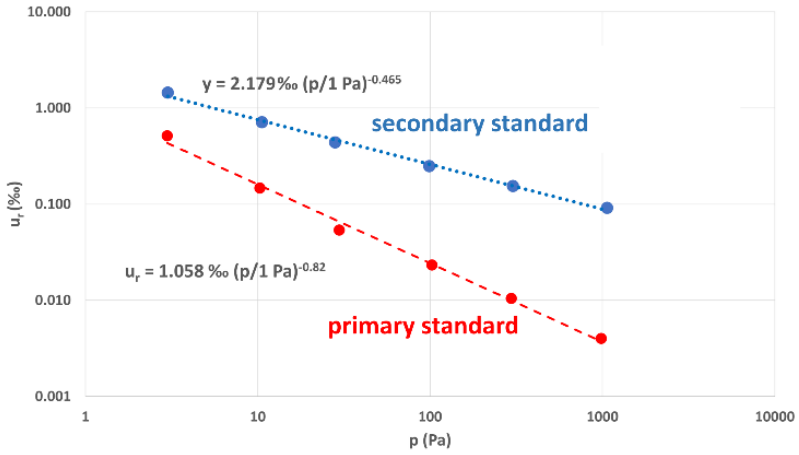

Fig. 5.2 Relative standard uncertainty of the transfer standard pressure gauge (blue) and the NIST primary standards to which it is traceable.

all measurements involved relatively low-pressure samples below 1 kPa, the measured CO spectra were dominated by Doppler broadening effects. Except for the relatively weak R28 transition (which was measured at a pressure of 830 Pa) the self-broadening contribution to the width of the lines was no greater than ~1% of the Doppler halfwidth. Likewise, far-wing and line-mixing effects involving nearby lines were negligible because of the low sample pressures employed. Using a Voigt profile (VP) with a linear baseline, the measured spectra could be fit with signal-to-noise ratios exceeding 10^4:1. See Fig. 5.3 for an example of a typical spectrum, Voigt fit and fit residuals showing no evidence of systematic structure. The parameters included the calculated Doppler width and three fitted quantities corresponding to the collisional width, peak location, and peak area of the VP.

Unlike the case for the other measured lines, we observed *w*-shaped residuals from fits of the VP to the R28 line spectra which can be ascribed to collisional (Dicke) narrowing of the line shape. Fitting the Galatry profile to these data (which models the collisional narrowing effect) eliminated the structured fit residuals and yielded a narrowing coefficient of $9.5(3)\times10^{-3}$ MHz Pa^{-1}. For comparison, we cite similar results from fits of the Galatry profile [33] to measurements of self-broadened $^{13}C^{16}O$ 3-0 band transitions given in [34]. They reported a density-based narrowing coefficient for the P28 transition of 0.298(15) GHz/(10^{19} molec. cm^{-3}) which at 296 K corresponds to a pressure-based value of $7.3(4)\times10^{-3}$ MHz Pa^{-1}.

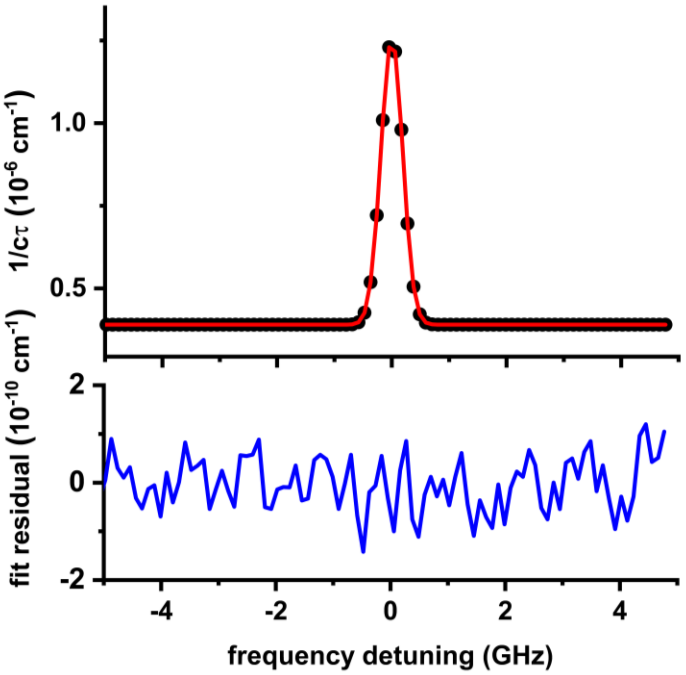

Figure. 5.3. Upper panel: measured CRDS spectrum (solid circles) and fitted Voigt profile (red line) for the R7 3-0 band transition of $^{12}C^{16}O$ at a pressure of ~2 Pa. Lower panel: fit residuals (obs. – fit). The peak signal-to-noise ratio is 16,500:1.

5.2 Uncertainty Analysis

In Table 5.2 we report the dominant statistical (Type A), and persistent or systematic (Type B), contributions to the uncertainties in the measured intensities. Because these measurements involve lines spanning a wide range of intensities (with the sample gas pressure adjusted to maintain similar peak absorption losses) and due to differences in the temperature dependence of the Boltzmann factors, the uncertainties in measured intensity vary substantially from line to line.

Five contributions to Type A uncertainty were considered. These components include a) the effect of variations in the pressure and b) temperature measurements within a spectrum acquisition, c) statistical uncertainty in the fitted peak area, d) uncertainty in measurement of the leak rate of air into the sample volume and e) fill-to-fill variation in pressure standard zero offset and CO partial pressure at $t = 0$. The fitted peak area term includes the effect of all noise sources in the frequency detuning (x-axis) and decay

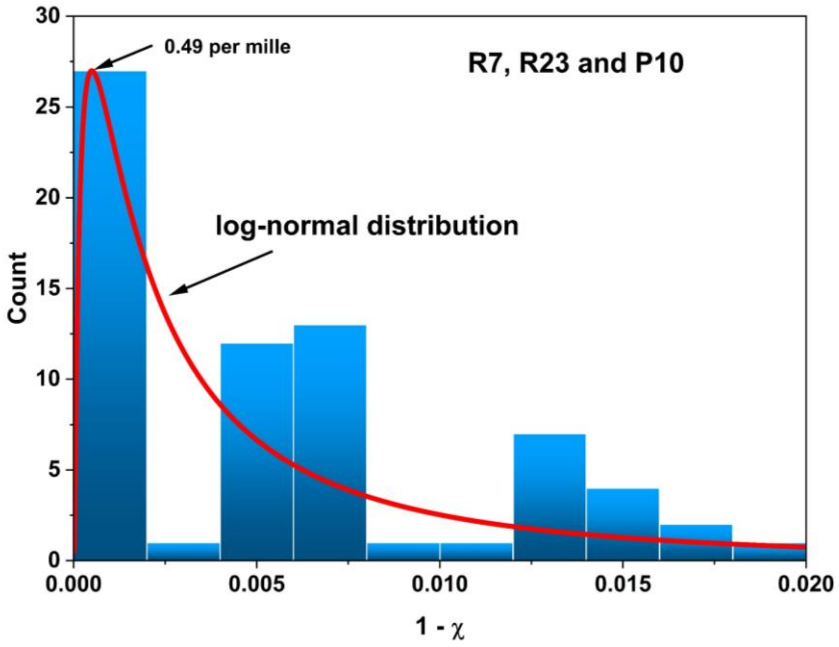

Figure 5.4. Distribution of normalized peak areas caused by uncertainty in fill-to-fill variations of the CO partial pressure for the R7, R23 and P10 lines. Here, χ, is the inferred change in the amount fraction of CO in the sample. We note that the data for the R23 line used in this dataset were acquired at a pressure 4.5 Pa. The indicated log-normal distribution (solid red line) is a fit to the data.

rate (y-axis) of the measured cavity ring-down spectra, and it includes uncertainties in the spectrum baseline. The first four sources of statistical variation contribute on average 0.2 ‰ to the data scatter. For a given fill, repeated measurements of spectrum areas have a relative standard deviation close to this value.

The largest source of statistical variability in the experiment was by far associated with uncertainty in correcting for changes in the zeros of the standard pressure gauges and the CO amount fraction (or partial pressure) at the beginning of each fill cycle (column e Table 5.2).

The dominant Type B uncertainty is associated with the fill-to-fill bias (see column f Table 5.2). We estimated this component in terms of the most-probable value of the log-normal distribution of inferred CO sample amounts. This quantity varies from line-to-line, scales inversely with the measurement pressure and has a maximum magnitude of 0.5 ‰. Expressed as relative uncertainties, these last two terms are inversely proportional to pressure. As illustrated in Fig. 5.4, we present the normalized distributions of measured $^{12}C^{16}O$ amount for the R7, R23 and P10 lines, (here the R23 line was measured over a wide range of pressures from 1.5 Pa to 100 Pa). This distribution exhibits an asymmetric shape with most-probable amount fractions, χ, that are slightly less than unity, where χ=1 would be expected in the absence of air leakage. The one-sided nature of this effect tends to make the measured intensities smaller than the true value, leading to a negative bias in our reported intensities especially for the strongest lines measured at the lowest pressures. We estimate the most-probable value of the bias to scale inversely with pressure range

Table 5.2. Relative standard uncertainty components in (‰) for all measured transitions. Columns a-e, Type A. Columns f-h, Type B. The last column, u_r, indicates the corresponding relative combined value for each transition. Column identifiers specifying sources of uncertainty: (a) measured pressure; (b) measured temperature; (c) spectroscopic fit; (d) variation in measured leak rate; (e) variation in pressure standard zero offset and CO partial pressure at t = 0; (f) fill-to-fill bias; (g) calibration uncertainty in pressure standard; (h) uncertainty in Boltzmann-factor temperature correction to 296 K; (u_r) relative combined standard uncertainty based on quadrature sum over all columns and including transition-independent uncertainties in the relative isotopologue abundance of $^{12}C^{16}O$ sample gas (0.12 ‰), sample impurity (0.05 ‰) and digitizer nonlinearity (0.1‰).

	a	b	c	d	e	f	g	h	u_r (‰)
P22	0.020	0.025	0.130	1.33×10^{-3}	0.494	0.010	0.029	0.50	0.764
P20	0.027	0.015	0.142	2.67×10^{-6}	0.571	0.020	0.038	0.30	0.742
P16	0.083	0.010	0.139	1.00×10^{-5}	0.464	0.075	0.109	0.20	0.779
P10	0.254	0.000	0.050	3.33×10^{-5}	0.537	0.250	0.354	0.00	1.159
P1	0.094	0.005	0.110	1.18×10^{-5}	0.947	0.088	0.127	0.10	1.142
R7	0.500	0.003	0.095	6.67×10^{-5}	0.922	0.500	0.708	0.06	1.760
R16	0.194	0.010	0.078	2.50×10^{-5}	0.509	0.188	0.266	0.20	1.045
R23	0.026	0.025	0.136	2.50×10^{-6}	0.379	0.019	0.037	0.50	0.722
R25	0.017	0.030	0.288	1.05×10^{-6}	0.377	0.008	0.023	0.60	0.806
R28	0.004	0.040	0.140	2.41×10^{-7}	0.445	0.002	0.006	0.80	0.946

from a minimum value of 2×10^{-3} ‰ in the best case (R28 line) to as much as 0.5 ‰ (R7 line) consistent with the distribution peak in Fig. 5.4.

Other systematic components of uncertainty include those associated with calibration of the standard pressure gauges (≤ 0.7 ‰), the Boltzmann-factor temperature correction (≤ 0.8 ‰) assuming $u(T)$ = 0.04 K combining contributions from the PRT calibration and temperature gradient, sample purity (0.05 ‰), nonlinear response of the digitizer used to record the ring-down decay signals (0.1 ‰) [31], as well as uncertainty in the isotopologue abundance of $^{12}C^{16}O$ (0.12 ‰) discussed below. The relative combined standard uncertainties for all lines are given in Table 9.1b and have an average value of 0.99 ‰.

5.3 Isotopic analysis

We determined the $^{12}C^{16}O$ (26) abundance, χ_{26}, by spectroscopically measuring peak areas for the pair of R7 ($^{13}C^{16}O$) and R23 ($^{12}C^{16}O$) 3-0 band transitions. The measured area ratio was $a_{R23}(^{12}C^{16}O)/\ a_{R7}(^{13}C^{16}O)$ = 3.7760(30) at T = 296 K. Because the detuning axes of our spectra were directly traceable to a recently calibrated Rb-stabilized OFC ($d\ln f_{RF}/dt \sim 5\times10^{-11}$ month^{-1}), we estimate that fractional biases in the peak areas associated with our measurement of optical frequency are at most 10^{-10} level, which can safely be neglected.

We assumed a stochastic distribution of C and O isotopes, and we specified $\delta^{18}O$ and $\delta^{17}O$ on the VSMOW scale corresponding to the reference values $(^{18}O/^{16}O)_{ref,VSMOW}$ = 0.0020052 [35] and $(^{17}O/^{16}O)_{ref,VSMOW}$ =3.799×10^{-4} [36]. In Fig. 5.5 we illustrate how $\Delta_{26} = \gamma_{26}/\gamma_{26,HT} - 1$ varies with $\delta^{13}C$ for three assumed values of $\delta^{18}O$. This quantity decreases linearly with increasing $\delta^{13}C$ and $\delta^{18}O$, and it exhibits partial derivatives of $d\Delta_{26}/d(\delta^{13}C) = -0.0111$ and $\Delta_{26}/d(\delta^{18}O) = -0.0020$, illustrating that Δ_{26} is much more sensitive to variations in $\delta^{13}C$ than it is to $\delta^{18}O$. Using HITRAN 2020 intensities for these lines [14] and setting $\delta^{18}O$ = 0 and $\delta^{17}O$ = –18.47 ‰ (consistent with HITRAN 2020 abundance ratio $^{17}O/^{16}O$), yields $\delta^{13}C$ = –35.6 ‰ (on the VPDB scale with a reference value of $^{13}C/^{12}C$ = 0.01118 [29]). These values lead to χ_{26} = 0.986985(118) for the isotopologue abundance of $^{12}C^{16}O$: a result that is 0.45 ‰ greater than the so-called natural abundance value of 0.986544 specified in HITRAN 2020 [14].

The uncertainty in χ_{26} was evaluated by summing three contributions: (1) relative uncertainty in the intensity ratio $u_r(S_{R7}/S_{R23})$ = 10 ‰, (2) uncertainty in the ^{18}O abundance, assumed to be $u(\delta^{18}O)$ = 25 ‰, and (3) relative uncertainty in the measured peak area ratio, $u_r(a_{R23}/a_{R7})$ = 0.79 ‰. To first order, the respective contributions introduce relative uncertainties in χ_{26} given by $\chi_{36}\times u_r(S_{R7}/S_{R23})$, $\chi_{28}\times u(\delta^{18}O)$ and

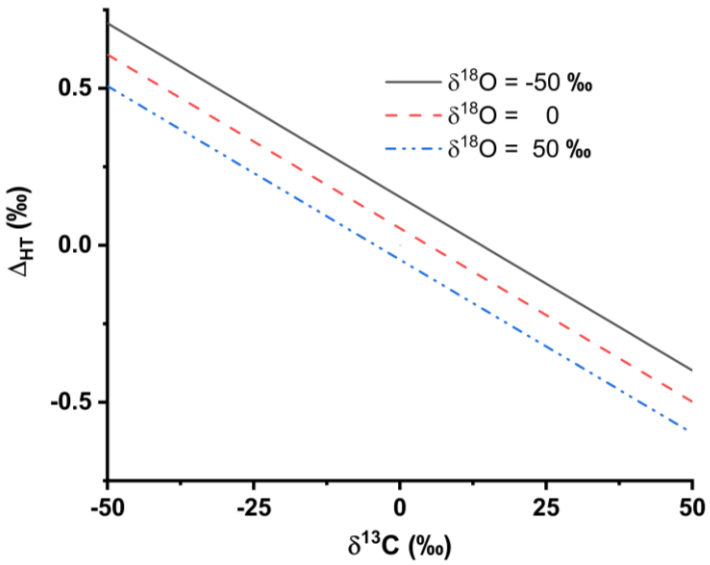

Figure 5.5. Normalized abundance of the $^{12}C^{16}O$ isotopologue, $\Delta_{26} = \gamma_{26}/\gamma_{26,HT} - 1$, as a function of the ^{13}C amount (VPDB scale) assuming a stochastic distribution of the stable C and O isotopes. Here, the subscript 26 refers to $^{12}C^{16}O$ and $\gamma_{26,HT}$ = 0.986544 is the natural abundance for the amount fraction of $^{12}C^{16}O$ from HITRAN 2020. The indicated $\delta^{18}O$ values are based on the VSMOW scale, and $\delta^{17}O$ is assumed to equal –18.47 ‰ (VSMOW), which corresponds to the relative abundance of $^{17}O/^{16}O$ specified in HITRAN 2020.

$\chi_{36} \times u_r(a_{R23}/a_{R7})$, where $\chi_{36} \sim 0.011$ and $\chi_{28} \sim 0.002$ are the nominal abundances of the second and third most abundant isotopologues. Adding these three components in quadrature gives a relative combined standard uncertainty of $u_r(\chi_{26}) = [(0.011\times10)^2 + (0.002\times25)^2 + (0.011\times0.79)^2]^{1/2}$ ‰ = 0.12 ‰.

6 Physikalische-Technische Bundesanstalt (PTB)

6.1 Description of Experiment and Uncertainties

The transmission spectrum of high-purity CO was recorded with a Fourier-transform spectroscopy (FTS) spectrometer. The configuration and experimental conditions are described in detail in Table 6.1.

The transmission spectrum was fitted with speed-dependent Voigt function, which is a limiting case of the Hartmann-Tran profile (HTP) [8], with first-order line-mixing coefficients incorporated and fixed to HITRAN 2020 [14] values. A third-order polynomial fit of the entire baseline was adopted, and the instrumental line shape (ILS) function was precisely determined from separate measurements of N_2O lines with the same spectrometer configuration. The fitted line intensities and relative combined standard uncertainties of the P22 to R22 lines scaled to 100 % abundance of $^{12}C^{16}O$ are presented in Table 9.1 b. The averaged relative combined standard uncertainty (approximately 1.3 ‰) of the retrieved line intensity is computed as the quadrature summation of pressure uncertainty (0.7 ‰), path length uncertainty (0.12 ‰), line area uncertainty (0.1 ‰ to 0.5 ‰), spectrum modeling (1 ‰), temperature uncertainty (0.01 ‰ to 0.2 ‰), sample isotopic composition (0.12 ‰), and sample purity (0.0025 ‰).

6.2 Determination of optical pathlength

The FTS spectrometer incorporated a three-mirror White-type multipass sample cell, having variable pathlengths ranging from nominally 3.2 m to 22.4 m. The optical pathlength within the sample was measured with a laser-based distance meter calibrated by a dimensional metrology group PTB, combined with ray tracing methods to account for the effects of beam divergence. These measurements and calculations yield relative standard uncertainties in pathlength from 0.6 ‰ to 0.15 ‰ for the 3.2 m and 22.4 m cases, respectively. In this study, the chosen configuration was 9.6919 m path with a standard relative uncertainty of 0.24 ‰.

Table 6.1: Experimental conditions for FTS measurements of CO 3-0 band at PTB.

Spectrometer configuration		
	Spectrometer	Bruker IFS 125HR
	IR Source	Tungsten / NIR
	Beam splitter	CaF_2
	Detector	RT-InGaAs
	Aperture	1.5 mm
	Optical filter	open
	FTS pressure	<0.0001 mbar
	Apodization	Boxcar
Measurement parameters		
	Resolution	0.012 cm^{-1}
	# of scans	500
	Averaging time	9 hours
	Gas used for ILS	N_2O
	Max SNR	4600
Gas cell		
	Type	White-type multipass cell
	Length as used	9.6919(23) m
	Windows	KBr wedged
	Temperature regulation	Julabo circulator
	Cell/sample temperature	295.96(5) K
	Pressure	10.158(7) kPa
Sample		
	CO	Linde Gas
	Purity	99.9995%

6.3 Determination of $^{12}C^{16}O$ isotopologue abundance

The relative abundances, χ_i of the three most abundant stable CO isotopologues $^{12}C^{16}O$ (26), $^{13}C^{16}O$ (36), and $^{12}C^{18}O$ (28), in the sample gas were determined spectroscopically from peak area ratios in the 3-0 band. The three least abundant isotopologues, $^{12}C^{17}O$ (27), $^{13}C^{18}O$ (38), $^{13}C^{17}O$ (37) were assumed to occur at the HITRAN 2020 abundances. The set of χ_i were calculated from these measurements assuming a stochastic distribution of C and O isotopes combined with HITRAN 2020 [14] line intensities. These measurements indicate that the sample was enriched in $^{12}C^{16}O$ by 0.74 ‰ compared to the HITRAN value of 0.98544 for this isotopologue. We also note that the $^{12}C^{18}O$ isotopologue was depleted by 18 ‰ relative to the corresponding HITRAN value. See Table 6.2 for a summary of these results.

Table 6.2: Experimental FTS measurements of CO isotopologue abundances. Uncertainties are based on relative uncertainties of 0.1 % for the intensity of $^{12}C^{16}O$, 1 % for the $^{13}C^{16}O$ and $^{12}C^{18}O$ intensities, and 5 % for the $^{12}C^{17}O$, $^{13}C^{18}O$ and $^{13}C^{17}O$ intensities.

isotopologue	26	36	28	27	38	37
χ_{HITRAN}	0.986544	0.011084	0.001978	3.6787E-4	2.2225E-5	4.1329E-6
χ_{meas}	0.987275	0.010389	0.001942	3.6787E-4	2.2225E-5	4.1329E-6
u_r (‰)	0.12	10.5	10.5	50	50	50

7. Sensitivity to temperature and comparison of FTS data from DLR and PTB

Line intensities follow a Boltzmann distribution in temperature, T, and depend on the lower state energy, E_J, and total internal partition function, $Q(T)$. The ratio of the intensity, $S(T)$, to that at a reference temperature, T_r, is given by [2]

$$\frac{S(T)}{S(T_r)} = \frac{Q(T_r)}{Q(T)} \frac{e^{-c_2 E_J/T}}{e^{-c_2 E_J/T_r}} \frac{[1-e^{(-c_2 \tilde{\nu}_{JJ'}/T)}]}{[1-e^{(-c_2 \tilde{\nu}_{JJ'}/T_r)}]}, \tag{7.1}$$

where $c_2 = hc/k$ = 1.43877688 … cm K and $\tilde{\nu}_{JJ'}$ is the wavenumber of the transition. For the wavenumber and temperature ranges considered here, the exponential terms within the brackets are negligible. Taking the natural logarithm of Eq. 7.1 and evaluating its first derivative we obtain the fractional change of intensity per unit temperature as,

$$\frac{d\ln(S)}{dT} = \left[\frac{c_2 E_J}{T_r^2} - \frac{d\ln(Q)}{dT}\right]. \tag{7.2}$$

As discussed in the Sec. 2.5 (Final Report Summary) and Sec. 3.2 (this document), measured intensities are based on experimental peak area determinations which are subsequently modeled as the product of two temperature-dependent quantities, namely line intensity and absorber number density scaling as $1/T$. Assuming small differences from the reference temperature, a first order expansion of $S(T)/T$ about T_r results in

$$\frac{d(S/T)}{dT} = \frac{1}{T}\left(\frac{dS}{dT} - \frac{S}{T}\right) = \frac{S}{T}\left(\frac{d\ln(S)}{dT} - \frac{1}{T}\right) = \frac{S}{T}\left[\frac{c_2 E_J}{T_r^2} - \frac{d\ln(Q)}{dT} - \frac{1}{T}\right], \tag{7.3}$$

so that correcting the measured intensity measured at temperature, T, to the value at the reference temperature, T_r, introduces a relative change in $S(T)/T$ of

$$\delta_{S/T}(T - T_r) = \frac{\left[\frac{S(T)}{T} - \frac{S(T_r)}{T_r}\right]}{\frac{S(T_r)}{T_r}} \approx \left[\frac{c_2 E_J}{T_r^2} - \frac{d\ln(Q)}{dT} - \frac{1}{T_r}\right](T - T_r). \tag{7.4}$$

This relation shows that the measured $S(T)/T$ will decrease with increasing temperature when $\left[\frac{c_2 E_J}{T_r^2} < \frac{d\ln(Q)}{dT} + \frac{1}{T}\right]$ and conversely it will increase with temperature for $\left[\frac{c_2 E_J}{T_r^2} > \frac{d\ln(Q)}{dT} + \frac{1}{T}\right]$. Note that in the absence of the gas density effect, the relative change in $S(T)$ with temperature, δ_S , can be evaluated with Eq. 7.4 by omitting the $1/T$ term in brackets.

To illustrate the magnitude of this effect, we calculated the temperature sensitivity with Eq. 7.4 for the 3-0 band of $^{12}C^{16}O$ assuming the standard reference temperature of 296 K and a temperature change of 0.1 K. We used the lower state energies from Table 8.1, and we evaluated the partition function and its derivative at 296 K using Python and the HAPI code [37] which gave Q = 107.42 and $\frac{d\ln(Q)}{dT}$ = 3.371×10^{-3} K^{-1}. The effect of gas density on retrieved $S(T)/T$ shifts $\delta_{S/T}$ down from δ_S by an amount 0.1 K/296 K = 0.34 ‰

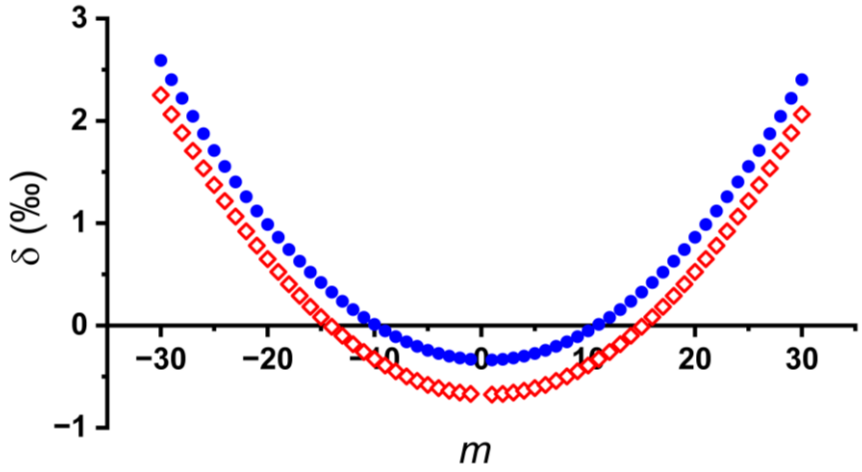

Figure 7.1. Sensitivity of the line intensity, $S(T)$ (blue dots), and the experimentally observed quantity, $S(T)/T$ (red diamonds), to a temperature increase of 0.1 K above the reference temperature at 296 K. Here m = -J (P branch) and m = J+1 (R branch).

for all m. The results, shown in Fig. 7.1, illustrate that for $J \leq 9$, $dS/dT < 0$ and $\delta_S < 0$. For higher rotational quantum numbers δ_S increases rapidly, approaching a value of 3 ‰ for the P30 and R31 transitions. Thus, high J intensities (greater than about 20) are extremely sensitive to temperature measurement bias, which can be a dominant source of systematic uncertainty in line intensity measurements. Achieving temperature uncertainties below 0.1 K poses significant technical challenges in relatively large FTS systems given temperature nonuniformities. In more compact cavity-enhanced setups, uncertainties as low as 0.01 K are more readily achieved- making these experiments even more suitable for the highest accuracy determination of weak high-J lines.

Because intensity data are typically corrected to 296 K it is useful to consider how such a correction would be in error given a bias in the measured temperature, T_m. For small temperature changes, this intensity correction from an arbitrary temperature, T, to the reference temperature can be estimated as above by a first order expansion of $S(T)/T$ as shown above.

However, in this case we assume that T_m is subject to systematic error and differs from the actual temperature, T, by a fixed amount, ΔT_{err}, *i.e.*, $\Delta T_{err} = T_m - T$. Using T_m to correct the measured intensity, $S(T)$ to $S(T_r)$ results in an apparent measured reference value of

$$\frac{S^{(app)}(T_r)}{T_r} = \frac{S(T)}{T} - (T_m - T_r)\frac{d(S/T)}{dT} \tag{7.5}$$

whereas using the corrected value of T_m gives the bias-corrected value,

$$\frac{S(T_r)}{T_r} = \frac{S(T)}{T} - (T_m - \Delta T_{err} - T_r)\frac{d(S/T)}{dT}\,. \tag{7.6}$$

Taking the difference between these two equations, we find that the relative bias in the line intensity at the reference condition becomes.

$$\frac{S^{(app)}(T_r) - S(T_r)}{S(T_r)} \approx -\Delta T_{err}\left[\frac{d\ln S}{dT} - \frac{1}{T}\right] \quad . \tag{7.7}$$

This equation shows that if both ΔT_{err} and $\frac{d\ln S}{dT} - \frac{1}{T}$ have the same sign, then the apparent intensity at the reference condition will be an underestimate of the correct value, otherwise it will be an overestimate. This property can be useful for determining the sign of potential temperature biases when comparing *m*-dependent trends in intensity data from different experiments.

As a specific example of temperature effects, the two data sets acquired using the FTS technique (i.e., those from DLR and PTB) provide the most comprehensive coverage over the range of *m* considered here, and consequently given enough precision these data make it possible to investigate potential *m*-dependent

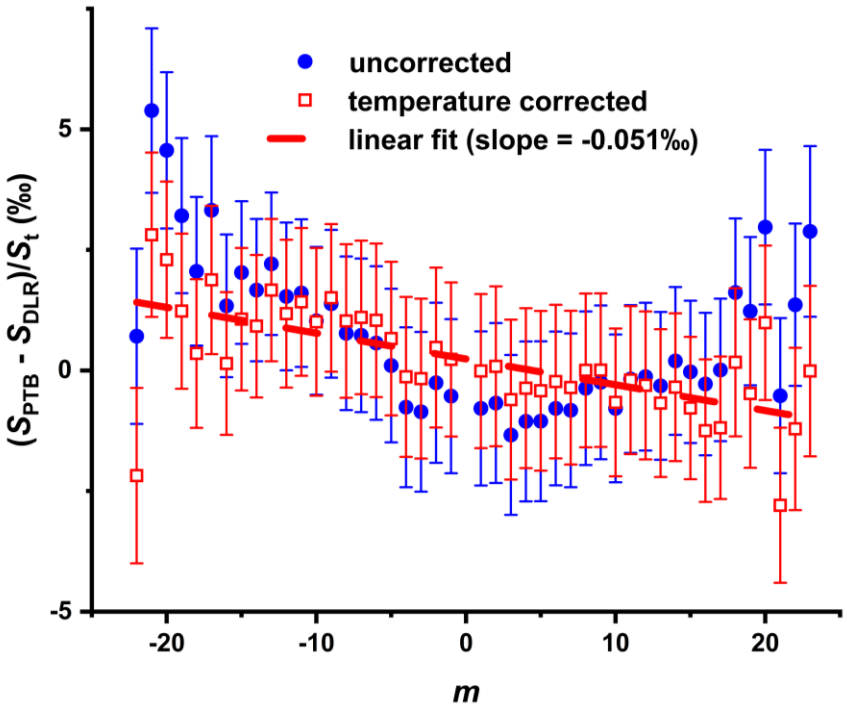

Figure 7.2. Differences between intensities measured by PTB and DLR normalized by the corresponding theoretical intensities given in Table 3. The temperature-corrected results (red open symbols) correspond to ΔT = 0.15 K for DLR and ΔT = -0.08 K for PTB, for which the dashed line is a linear regression to these data. The error bars are given by the combined uncertainties for the two sets of data. The average of the temperature-corrected data is 0.2 ‰, with a standard deviation of 1.1‰.

measurement biases driven by biases in measurements of sample temperature. As can be seen in Fig. 7.2,

there are systematic deviations between these two sets of intensities that vary with rotational quantum number *m*- specifically corresponding to a nominally quadratic dependence on *m*- a trend that we attribute to increasing sensitivity of the measured intensity to variation in sample temperature as shown in Fig. 7.1. Empirically, we find that any combination of positive- or negative-going temperature corrections (using Eq. 7.2) in the DLR (PTB) data equaling about 0.23 K (which is about twice the combined uncertainty of the two experimental temperature determinations equal to 0.11 K), reduces the *m*-dependent deviation in the intensities. This *ad hoc* correction results in an average relative difference of 0.2 ‰ with a standard deviation of 1.1 ‰ for these two FTS-based data sets. Nevertheless, after this adjustment there remains a small linear dependence on *m* in the measured intensities. This residual trend has a slope of 0.051 ‰ per unit *m*, thus seeming to correlate with wavelength or frequency. However, we have no good physical explanation for this result.

8. Rotational assignments, transition frequencies, and lower state energies, with theoretical and measured intensities.

Table 8.1. Ancillary data used in the spectrum modelling of the $^{12}C^{16}O$ (3-0) band. The branch (*P* or *R*) and rotational assignments, *J* and *m*, transition wavenumbers, $\tilde{\nu}$, and lower-state energies, E_J, are taken from HITRAN 2020 [14].

#	branch	J	m	$\tilde{\nu}$ (cm^{-1})	E_J/hc (cm^{-1})
1	P	22	-22	6241.8512	971.2332
2	P	21	-21	6247.8675	886.9024
3	P	20	-20	6253.7819	806.3828
4	P	19	-19	6259.5942	729.6774
5	P	18	-18	6265.3043	656.7892
6	P	17	-17	6270.9120	587.7209
7	P	16	-16	6276.4173	522.4751
8	P	15	-15	6281.8198	461.0544
9	P	14	-14	6287.1195	403.4612
10	P	13	-13	6292.3163	349.6975
11	P	12	-12	6297.4100	299.7656
12	P	11	-11	6302.4005	253.6672
13	P	10	-10	6307.2875	211.4041
14	P	9	-9	6312.0710	172.978
15	P	8	-8	6316.7508	138.3904
16	P	7	-7	6321.3268	107.6424
17	P	6	-6	6325.7989	80.7354
18	P	5	-5	6330.1667	57.6704
19	P	4	-4	6334.4303	38.4481
20	P	3	-3	6338.5895	23.0695
21	P	2	-2	6342.6441	11.535
22	P	1	-1	6346.5940	3.845
23	R	0	1	6354.1791	0
24	R	1	2	6357.8140	3.845
25	R	2	3	6361.3435	11.535

26	R	3	4	6364.7676	23.0695
27	R	4	5	6368.0861	38.4481
28	R	5	6	6371.2989	57.6704
29	R	6	7	6374.4058	80.7354
30	R	7	8	6377.4066	107.6424
31	R	8	9	6380.3013	138.3904
32	R	9	10	6383.0896	172.978
33	R	10	11	6385.7715	211.4041
34	R	11	12	6388.3467	253.6672
35	R	12	13	6390.8152	299.7656
36	R	13	14	6393.1767	349.6975
37	R	14	15	6395.4312	403.4612
38	R	15	16	6397.5784	461.0544
39	R	16	17	6399.6184	522.4751
40	R	17	18	6401.5508	587.7209
41	R	18	19	6403.3755	656.7892
42	R	19	20	6405.0925	729.6774
43	R	20	21	6406.7016	806.3828
44	R	21	22	6408.2025	886.9024
45	R	22	23	6409.5952	971.2332
46	R	23	24	6410.8796	1059.372
47	R	25	26	6413.1225	1247.059
48	R	28	29	6415.6704	1557.061

Table 8.2 Theoretical intensities, $S^{(t)}$, as reported in Bielska et al. [18], weighted-mean intensities measured in this work, $\bar{S}_m$, and the corresponding fitted intensities $S_m^{(fit)}$. Intensity values are in (cm^2 cm^{-1} molecule^{-1}) and correspond to 100 % $^{12}C^{16}O$ at T = 296 K. $u_r(\bar{S}_m)$ is the relative standard uncertainty in (‰) and N_L is the number of laboratories contributing to each reported intensity. The shaded cells correspond to transitions in the overlap set.

#	branch	J	m	$S^{(t)}$	$\bar{S}_m$	$u_r(\bar{S}_m)$	$S_m^{(fit)}$	N_L
1	P	22	-22	6.5066E-25	6.4992E-25	0.470	6.4978E-25	5
2	P	21	-21	9.4640E-25	9.4572E-25	0.847	9.4524E-25	2
3	P	20	-20	1.3483E-24	1.3469E-24	0.456	1.3468E-24	5
4	P	19	-19	1.8810E-24	1.8798E-24	0.788	1.8791E-24	2
5	P	18	-18	2.5689E-24	2.5654E-24	0.738	2.5667E-24	2
6	P	17	-17	3.4335E-24	3.4314E-24	0.736	3.4308E-24	2
7	P	16	-16	4.4893E-24	4.4862E-24	0.447	4.4862E-24	5
8	P	15	-15	5.7393E-24	5.7367E-24	0.680	5.7359E-24	2
9	P	14	-14	7.1706E-24	7.1649E-24	0.680	7.1670E-24	2
10	P	13	-13	8.7491E-24	8.7433E-24	0.680	8.7454E-24	2
11	P	12	-12	1.0417E-23	1.0412E-23	0.736	1.0413E-23	2

12	P	11	-11	1.2089E-23	1.2095E-23	0.736	1.2086E-23	2
13	P	10	-10	1.3658E-23	1.3654E-23	0.511	1.3655E-23	5
14	P	9	-9	1.4995E-23	1.4998E-23	0.736	1.4993E-23	2
15	P	8	-8	1.5960E-23	1.5967E-23	0.783	1.5959E-23	2
16	P	7	-7	1.6413E-23	1.6416E-23	0.783	1.6413E-23	2
17	P	6	-6	1.6229E-23	1.6236E-23	0.783	1.6230E-23	2
18	P	5	-5	1.5313E-23	1.5312E-23	0.783	1.5315E-23	2
19	P	4	-4	1.3616E-23	1.3614E-23	0.830	1.3618E-23	2
20	P	3	-3	1.1140E-23	1.1136E-23	0.830	1.1142E-23	2
21	P	2	-2	7.9519E-24	7.9442E-24	0.830	7.9538E-24	2
22	P	1	-1	4.1785E-24	4.1739E-24	0.523	4.1797E-24	5
23	R	0	1	4.3642E-24	4.3613E-24	0.786	4.3656E-24	2
24	R	1	2	8.6740E-24	8.6682E-24	0.830	8.6772E-24	2
25	R	2	3	1.2691E-23	1.2692E-23	0.830	1.2696E-23	2
26	R	3	4	1.6201E-23	1.6198E-23	0.830	1.6207E-23	2
27	R	4	5	1.9030E-23	1.9040E-23	0.827	1.9038E-23	2
28	R	5	6	2.1063E-23	2.1073E-23	0.783	2.1071E-23	2
29	R	6	7	2.2247E-23	2.2261E-23	0.786	2.2256E-23	2
30	R	7	8	2.2592E-23	2.2588E-23	0.586	2.2601E-23	5
31	R	8	9	2.2168E-23	2.2181E-23	0.786	2.2177E-23	2
32	R	9	10	2.1087E-23	2.1101E-23	0.736	2.1095E-23	2
33	R	10	11	1.9491E-23	1.9499E-23	0.736	1.9498E-23	2
34	R	11	12	1.7538E-23	1.7546E-23	0.736	1.7544E-23	2
35	R	12	13	1.5382E-23	1.5388E-23	0.736	1.5387E-23	2
36	R	13	14	1.3164E-23	1.3168E-23	0.736	1.3168E-23	2
37	R	14	15	1.1002E-23	1.1007E-23	0.680	1.1005E-23	2
38	R	15	16	8.9852E-24	8.9892E-24	0.680	8.9871E-24	2
39	R	16	17	7.1752E-24	7.1771E-24	0.482	7.1764E-24	5
40	R	17	18	5.6050E-24	5.6074E-24	0.736	5.6057E-24	2
41	R	18	19	4.2847E-24	4.2845E-24	0.736	4.2850E-24	2
42	R	19	20	3.2063E-24	3.2080E-24	0.788	3.2064E-24	2
43	R	20	21	2.3494E-24	2.3476E-24	0.790	2.3493E-24	2
44	R	21	22	1.6861E-24	1.6851E-24	0.839	1.6859E-24	2
45	R	22	23	1.1854E-24	1.1858E-24	0.886	1.1852E-24	2
46	R	23	24	8.1663E-25	8.1656E-25	0.512	8.1643E-25	5
47	R	25	26	3.6481E-25	3.6464E-25	0.584	3.6466E-25	4
48	R	28	29	9.3839E-26	9.3819E-26	0.601	9.3776E-26	5

9. Summary of measured intensities and uncertainties reported by each laboratory

Table 9.1a. Reported intensities ($cm^2\ cm^{-1}\ molecule^{-1}$) for 100 % $^{12}C^{16}O$ and relative combined standard uncertainties (‰) for DLR, KRISS and NCU.

	DLR			KRISS			NCU	
m	***S***	u_r		***S***	u_r		***S***	u_r
-22	6.4948E-25	1.21		6.5587E-25	25.5		6.4932E-25	0.84
-21	9.4379E-25	1.11						
-20	1.3455E-24	1.01					1.3453E-24	0.90
-19	1.8778E-24	1.01						
-18	2.5640E-24	0.91						
-17	3.4280E-24	0.91						
-16	4.4844E-24	0.81					4.4824E-24	0.96
-15	5.7341E-24	0.81						
-14	7.1624E-24	0.81						
-13	8.7389E-24	0.81						
-12	1.0409E-23	0.91						
-11	1.2090E-23	0.91						
-10	1.3658E-23	0.91					1.3642E-23	0.95
-9	1.4993E-23	0.91						
-8	1.5965E-23	1.01						
-7	1.6414E-23	1.01						
-6	1.6236E-23	1.01						
-5	1.5314E-23	1.01						
-4	1.3621E-23	1.11						
-3	1.1143E-23	1.11						
-2	7.9469E-24	1.11						
-1	4.1747E-24	1.01					4.1754E-24	0.95
1	4.3635E-24	1.01						
2	8.6727E-24	1.11						
3	1.2702E-23	1.11						
4	1.6209E-23	1.11						
5	1.9053E-23	1.11						
6	2.1084E-23	1.01						
7	2.2273E-23	1.01						
8	2.2611E-23	1.01					2.2578E-23	1.09
9	2.2188E-23	1.01						
10	2.1110E-23	0.91						
11	1.9504E-23	0.91						
12	1.7550E-23	0.91						
13	1.5392E-23	0.91						
14	1.3169E-23	0.91						

15	1.1008E-23	0.81						
16	8.9913E-24	0.81						
17	7.1771E-24	0.81					7.1793E-24	0.95
18	5.6053E-24	0.91						
19	4.2834E-24	0.91						
20	3.2049E-24	1.01						
21	2.3486E-24	1.01						
22	1.6845E-24	1.11						
23	1.1845E-24	1.21						
24	8.1621E-25	1.31		8.0182E-25	5.5		8.1652E-25	0.94
26				3.4780E-25	11.0		3.6477E-25	0.88
29	9.3800E-26	2.20		9.3370E-26	14.5		9.3828E-26	0.89

Table 9.1b. Reported intensities ($cm^2\ cm^{-1}\ molecule^{-1}$) for 100 % $^{12}C^{16}O$ and relative combined standard uncertainties (‰) for NIM, NIST and PTB.

	NIM			NIST			PTB	
m	***S***	u_r		***S***	u_r		***S***	u_r
-22	6.5199E-25	2.21		6.5032E-25	0.77		6.4961E-25	1.37
-21							9.4841E-25	1.31
-20	1.3479E-24	2.24		1.3470E-24	0.75		1.3510E-24	1.28
-19							1.8829E-24	1.26
-18							2.5680E-24	1.26
-17							3.4377E-24	1.25
-16	4.5087E-24	2.55		4.4866E-24	0.79		4.4881E-24	1.25
-15							5.7428E-24	1.25
-14							7.1708E-24	1.25
-13							8.7538E-24	1.25
-12							1.0419E-23	1.25
-11							1.2103E-23	1.25
-10	1.3673E-23	2.82		1.3649E-23	1.16		1.3665E-23	1.25
-9							1.5006E-23	1.25
-8							1.5970E-23	1.24
-7							1.6418E-23	1.24
-6							1.6237E-23	1.24
-5							1.5308E-23	1.24
-4							1.3604E-23	1.25
-3							1.1128E-23	1.25
-2							7.9408E-24	1.25
-1	4.1922E-24	2.40		4.1686E-24	1.15		4.1704E-24	1.25
1							4.3579E-24	1.25
2							8.6625E-24	1.25
3							1.2679E-23	1.25
4							1.6184E-23	1.25
5							1.9023E-23	1.24
6							2.1057E-23	1.24
7							2.2243E-23	1.25
8	2.2526E-23	2.83		2.2558E-23	1.76		2.2591E-23	1.25
9							2.2171E-23	1.25
10							2.1083E-23	1.25
11							1.9491E-23	1.25
12							1.7539E-23	1.25
13							1.5380E-23	1.25
14							1.3165E-23	1.25
15							1.1003E-23	1.25

16							8.9843E-24	1.25
17	7.1802E-24	2.82		7.1749E-24	1.05		7.1736E-24	1.25
18							5.6115E-24	1.25
19							4.2865E-24	1.25
20							3.2128E-24	1.26
21							2.3461E-24	1.27
22							1.6860E-24	1.28
23							1.1873E-24	1.30
24	8.1696E-25	2.14		8.1651E-25	0.73			
26	3.6250E-25	2.53		3.6467E-25	0.82			
29	9.3955E-26	2.29		9.3768E-26	0.95			

References for Supplemental Material:

1. Gamache, R.R., et al., *Total internal partition sums for the HITRAN2020 database*. Journal of Quantitative Spectroscopy & Radiative Transfer, 2021. **271**.
2. Rothman, L.S., et al., *The HITRAN molecular spectroscopic database and HAWKS (HITRAN Atmospheric Workstation): 1996 edition.* Journal of Quantitative Spectroscopy & Radiative Transfer, 1998. **60**(5): p. 665-710.
3. Yariv, A., *Quantum electronics*. 3rd ed ed. 1989: Wiley.
4. Busch, K.W., et al., *Cavity-ringdown spectroscopy : an ultratrace-absorption measurement technique*. ACS symposium series 720. 1999, Washington, District of Columbia: American Chemical Society.
5. Libbrecht, K.G. and M.W. Libbrecht, *Interferometric measurement of the resonant absorption and refractive index in rubidium gas.* American Journal of Physics, 2006. **74**(12): p. 1055-1060.
6. Cygan, A., et al., *One-dimensional frequency-based spectroscopy.* Optics Express, 2015. **23**(11): p. 14472-14486.
7. Siegel, R. and J.R. Howell, *Thermal radiation heat transfer*. 1981, Washington, D.C: Hemisphese.
8. Ngo, N.H., et al., *An isolated line-shape model to go beyond the Voigt profile in spectroscopic databases and radiative transfer codes.* Journal of Quantitative Spectroscopy & Radiative Transfer, 2013. **129**: p. 89-100.
9. Tennyson, J., et al., *Recommended isolated-line profile for representing high-resolution spectroscopic transitions (IUPAC Technical Report).* Pure and Applied Chemistry, 2014. **86**(12): p. 1931-1943.
10. Birk, M., C. Roeske, and G. Wagner, *High accuracy COFourier transform measurements in the range 6000-7000 cm.* Journal of Quantitative Spectroscopy & Radiative Transfer, 2021. **272**.
11. Tran, H., et al., *Non-impact effects in the absorption spectra of HCl diluted in CO, air, and He: Measurements and predictions.* Journal of Chemical Physics, 2023. **158**(18).
12. Reed, Z.D., et al., *SI-traceable molecular transition frequency measurements at the 10^{-12} relative uncertainty level.* Optica, 2020. **7**(9): p. 1209-1220.
13. Cygan, A., et al., *High-accuracy and wide dynamic range frequency-based dispersion spectroscopy in an optical cavity.* Optics Express, 2019. **27**(15): p. 21811-21822.
14. Gordon, I.E., et al., *The HITRAN2020 molecular spectroscopic database.* Journal of Quantitative Spectroscopy & Radiative Transfer, 2022. **277**.
15. Bevington, P.R. and D.K. Robinson, *Data reduction and error analysis for the physical sciences*. 2nd ed. McGraw-Hill international editions: physics series. 1992, New York: McGraw-Hill. xvii, 328 pages : illustrations.

16. Altman, D.G. and J.M. Bland, *Standard deviations and standard errors.* BMJ, 2005. **331**(7521): p. 903.
17. Balashov, A.A., et al., *Measurement and calculation of CO (7-0) overtone line intensities.* J Chem Phys, 2023. **158**(23).
18. Bielska, K., et al., *Subpromille Measurements and Calculations of CO (3-0) Overtone Line Intensities.* Physical Review Letters, 2022. **129**(4).
19. Reed, Z.D., et al., *Effect of Non-Markovian Collisions on Measured Integrated Line Shapes of CO.* Physical Review Letters, 2023. **130**(14).
20. Watson, J.K.G., *Quadratic Herman-Wallis Factors in the Fundamental Bands of Linear-Molecules.* Journal of Molecular Spectroscopy, 1987. **125**(2): p. 428-441.
21. *Brand names are mentioned solely for informational purposes and are not to be understood as a product endorsement by any of the parties involved in this research.*
22. Birk, M., *et al.. The pressure dependence of the experimentally determined line intensity and continuum absorption of pure CO2 in the 1.6 μm region.* Journal Quantitative Spectroscopy and Radiative Transfer, 2024. **324**: p. 109055.
23. Lisak, D., et al., *Dual-comb cavity ring-down spectroscopy.* Scientific Reports, 2022. **12**(1).
24. Long, D.A., et al., *Frequency-agile, rapid scanning spectroscopy: absorption sensitivity of 2 x 10 cm^{-1} $Hz^{-1/2}$ with a tunable diode laser.* Applied Physics B-Lasers and Optics, 2014. **114**(4): p. 489-495.
25. Cygan, A., et al., *Absolute molecular transition frequencies measured by three cavity-enhanced spectroscopy techniques.* Journal of Chemical Physics, 2016. **144**(21).
26. Cygan, A., *et. al, Heterodyne dispersive cavity ring-down spectroscopy exploiting eigenmode frequencies for high-fidelity measurements, in preparation.* 2024.
27. Guo, R.M., et al., *Comb-assisted, Pound-Drever-Hall locked cavity ring-down spectrometer for high-performance retrieval of transition parameters.* Optics Express, 2019. **27**(22): p. 31850-31863.
28. Guo, R.M., et al., *Line parameters of the P-branch of (30012) ← (00001) CO band measured by comb-assisted, Pound-Drever-Hall locked cavity ring-down spectrometer.* Journal of Quantitative Spectroscopy & Radiative Transfer, 2021. **264**.
29. Zhang, Q.L., T.L. Chang, and W.J. Li, *A Calibrated Measurement of the Atomic-Weight of Carbon.* Chinese Science Bulletin, 1990. **35**(4): p. 290-296.
30. Brand, W.A., S.S. Assonov, and T.B. Coplen, *Correction for the O interference in δ(C) measurements when analyzing COwith stable isotope mass spectrometry (IUPAC Technical Report).* Pure and Applied Chemistry, 2010. **82**(8): p. 1719-1733.
31. Fleisher, A.J., et al., *Twenty-Five-Fold Reduction in Measurement Uncertainty for a Molecular Line Intensity.* Physical Review Letters, 2019. **123**(4).
32. Hendricks, J.H. and D.A. Olson, *1-15,000 Pa Absolute mode comparisons between the NIST ultrasonic interferometer manometers and non-rotating force-balanced piston gauges.* Measurement, 2010. **43**(5): p. 664-674.
33. Galatry, L., *Simultaneous Effect of Doppler and Foreign Gas Broadening on Spectral Lines.* Physical Review, 1961. **122**(4): p. 1218-&.
34. Wójtewicz, S., et al., *Low pressure line-shape study of self-broadened CO transitions in the (3←0) band.* Journal of Quantitative Spectroscopy & Radiative Transfer, 2013. **130**: p. 191-200.
35. Baertschi, P., *Absolute O-18 Content of Standard Mean Ocean Water.* Earth and Planetary Science Letters, 1976. **31**(3): p. 341-344.
36. Li, W., Baoling, N., Dequi, J., Qinglian, Z., *Measurement of the absollute abundance of oxygen-17 in VSMOW.* Kexue Tongbao (Chinese Science Bulletin, 1988. **33**: p. 4.
37. Kochanov, R.V., et al., *HITRAN Application Programming Interface (HAPI): A comprehensive approach to working with spectroscopic data.* Journal of Quantitative Spectroscopy & Radiative Transfer, 2016. **177**: p. 15-30.